nature communications

Article

https://doi.org/10.1038/s41467-025-67364-6

Prodrug nanoplatform for triggering ferroptosis to eliminate senescent cells in age-associated pathologies

Received: 21 February 2025

Accepted: 27 November 2025

Published online: 13 December 2025

Check for updates

Chengkang Jin[1,2,8], Xiaoling Xu[1,3,8] ✉, Ning Yao[4], Hairui Zhang[5], Changjiang Chen[6], Lingyao Zeng[1,3], Zhiyun Liu[1,3], Lanjie Lei[1], Shumao Cui[7], Chengping Wen[2] ✉ & Liyun Shi[1] ✉

Accumulation of senescent cells is associated with aging and age-related diseases. However, current clearance therapies targeting senescent cells are often limited by low efficiency, poor specificity, and insufficient penetration. Here we develop a nano-platform composed of a probe (GD) that can be specifically activated by senescent cells, a photosensitizer (Ce6), and a peptide (HK) for targeting ferritin, named HK-PCGC. We show that upon entering senescent cells, GD is activated by high levels of β-galactosidase, releasing fluorescence to excite Ce6. Ce6 then generates reactive oxygen species to eliminate these cells. Additionally, we find that under the guidance of the peptide HK, our system degrades ferritin to trigger ferroptosis, further eliminating senescent cells. Collectively, we demonstrate that HK-PCGC can effectively eliminate senescent cells, reduce the senescence-associated secretory phenotype, and safely improve the physical fitness of aged mice. This study integrates senescent cell responsiveness, laser-free photodynamic therapy, and induction of ferroptosis, offering a potential approach for delaying aging.

Aging is an irreversible process with the decline in tissue function and physical activity, and is thought to contribute to the development of degenerative diseases such as Alzheimer's disease, cardiovascular diseases, cancer, and age-related macular degeneration and arthritis[1,2]. Although the underlying mechanisms are not completely elucidated, cellular senescence has been appreciated as a core event underpinning progressive aging. Senescence is a cellular state characterized by cell cycle arrest and the secretome enriched in proinflammatory cytokines and extracellular matrix proteins, namely senescence-associated secretory phenotype (SASP)[3]. Senescence is also accompanied by disturbed organelle functions, such as distorted mitochondria, stressed endoplasmic reticulum, and defective lysosomes that are characterized by impaired degradative capability and highly expression of senescence-associated β-galactosidase (β-Gal)[4]. Despite benefiting some of biological activities like wound healing and embryogenesis, excessively accumulated senescent cells (SnCs) have been implicated in aging and age-associated diseases[5]. Selective eradication of SnCs is therefore regarded as an attractive approach to delay aging and alleviate age-associated pathologies[6–8].

Recently, a number of senolytic agents such as dasatinib and quercetin (DQ)[9], ABT-263/737[10], HSP90 inhibitor[11], cardiac glycoside[12] and procyanidin C1[13] have been discovered and demonstrated promising results in both pre-clinical and clinical trials. However, they still face challenges such as limited specificity and therapeutic efficacy,

[1]Key Laboratory of Artificial Organs and Computational Medicine in Zhejiang Province, Institute of Translational Medicine, Zhejiang Shuren University, Hangzhou, Zhejiang, China. [2]College of Basic Medical Science, Zhejiang Chinese Medical University, Hangzhou, China. [3]Shulan International Medical College, Zhejiang Shuren University, Hangzhou, China. [4]Department of General Surgery, Joint Support Force 903th Hospital, Hangzhou, China. [5]School of Pharmaceutical Sciences, Zhejiang Chinese Medical University, Hangzhou, China. [6]Department of Immunology and Medical Microbiology, Nanjing University of Chinese Medicine, Nanjing, China. [7]State Key Laboratory of Food Science and Resources, Jiangnan University, Wuxi, Jiangsu, China. [8]These authors contributed equally: Chengkang Jin, Xiaoling Xu. ✉e-mail: ziyao1988@zju.edu.cn; wengcp@163.com; sly0202@zjsru.edu.cn

unsatisfactory biocompatibility, and adverse effects[14]. Since most of current senotherapies are designed to target apoptotic pathways that also exist in normal cells, the off-target effects and potential cytotoxicity are inevitable. The development of a new generation of senolytics toward the non-apoptotic pathway is therefore of particular significance.

Ferroptosis is a newly identified non-apoptotic form of cell death driven by excessive lipid peroxides (LPO) and labile iron accumulation[15]. As is known, LPO is catalyzed by intracellular iron or lipoxygenases and cytochrome P450 oxidoreductase, leading to its deposition in the biomembrane to increase membrane permeability and hence initiate the process of cell death. In addition to reinvigorating LPO generation, labile iron ions also converts H_2O_2 to toxic hydroxyl radical (OH•), which in turn attacks polyunsaturated fatty acid (PUFA) and related phospholipids to promote lipid peroxidation and hence induce cellular ferroptosis[16]. Thus, LPO and intracellular bioactive iron constitute the major driving force for ferroptosis, and also the vulnerable targets for ferroptosis[17]. Recently, ferroptosis-based therapy has demonstrated encouraging results in combating cancers, but its potential as a senolytic treatment is yet to be explored[18–20].

Of interest, studies have shown that SnCs are characterized by iron accumulation even with lower levels extracellular iron, and senescence-inducing insults can provoke progressive iron accumulation. In accordance, overload of intracellular iron is causatively associated with senescent transformation and age-associated pathologies, such as fibrosis, metabolic disorders and cognitive decline[21–23]. The data thus indicate the intrinsic vulnerability of SnCs and suggest that induction of ferroptosis might be a promising approach to selective ablate SnCs[24]. However, there are still some critical issues to be addressed to exert the ferroptosis program in senescent cells. Firstly, it is currently known that under physiological conditions, intracellular iron is mostly sequestered by the ferritin nanocages, and the bound iron is only released upon autophagic degradation of ferritin, termed ferritinophagy. Since SnCs are generally featured with defective lysosome activity and hence compromised ferritinophagy, it is expected that labile iron in senescent cells is essentially entrapped in the storing cage[21,23]. Thus, promoting ferritin degradation to unleash the bound iron is perceived as a promising way for re-sensitizing SnCs to ferroptosis. Indeed, compared with current ferrotherapies that act mostly through delivery of exogenous iron or ferroptosis inducers, the strategy to induce cellular intrinsic ferrotosis outperforms them with lower systemic toxicity, increased cell selectivity and good biocompatibility[18].

Another hindrance for the induction of ferroptosis in SnCs is the insufficient supply of reactive oxygen species (ROS), a critical mediator for both LPO generation and bioactive iron release. This is paradoxical seemingly since SnCs are generally thought to be linked with oxidative stress and increased ROS production promotes cellular senescence. To resolve this contradiction, recent data indicate that, despite increased ROS production in SnCs, the reactive free radicals (HO• and RO•) are not sufficiently generated, and hence they impede LPO production and iron release by ferritinophagy[25]. Based on these findings, an integrated system that can simultaneously produce high levels of damaging radicals and labile iron is imperative to develop a senotherapy driven by endogenous ferroptosis.

Photodynamic therapy (PDT) is a dynamic and effective approach with the ability to generate great ROS and radicals via light-irradiated excitation of photosensitizer (PS)[26]. It has been clinically approved to treat some kinds of cancers and other conditions, and its therapeutic potential in combating SnCs has been recently investigated by a pilot study[27,28]. However, the relevant problems associated with traditional PDT, such as cell selectivity, treatment efficacy and bilateral toxicity need to be addressed before its wide application[29,30]. Moreover, the poor tissue penetration depths of light irradiation substantially impede the development of PDT as a new senolytic therapy, since senescent cells are equally distributed in the internal organs and in superficial organs like the skin. In this regard, a laser-free PDT provides an attractive option, as it can excite the internal light emission without external light input to exert the therapeutic effects[31,32]. Technically, the chemiluminescence has demonstrated superior ability to incite the photosensitizer such as chlorin e6 (Ce6) via chemiluminescence resonance energy transfer (CRET), and subsequently enabled it to produce cytotoxic $^1O_2$ with a large Stokes shift. As such, the self-illuminating approach provides a promising module for both in vivo imaging and enhanced therapy in deeper tissues, making it an ideal strategy for the new generation of senolytic treatments[33].

Although it has multiple merits, the self-powered PDT system still needs to address the issue of lower cell specificity. In our system, a β-Gal-responsive glycoprobe that conjugates a galactose moiety with adamantane-dioxetane is applied, which enables the on-site action of chemiluminescent reaction and subsequent CRET to mediate specific killing of senescent cells[34,35]. Furthermore, to precisely initiate ferroptosis-driven senotherapy, the PDT system is also equipped with cleaved high molecular weight kininogen (HKa), which serves as a ferritin-homing protein to direct the internalized PDT complex toward the ferritin cage, inducing ROS burst and simultaneously triggering ferritin degradation for iron release[18,36]. Lastly, to increase the sensitivity and efficiency of the PDT system, the SnC-responsive signal sensor is considered to associate with the CRET machinery in a confined space. For this, the macrocyclic host molecule, calixarene, attracts increasing attention as it can efficiently load and assemble the hydrophobic guest compounds to form various nanostructures. Moreover, the macrocyclic substance demonstrates low cytotoxicity, adjustable structure, readiness for functionalization and responsiveness to external stimuli, making it a promising drug carrier platform[37,38].

In this study, we devised a nanosenolytic (HK-PCGC) by incorporating the β-Gal-activatable GD probe, the photosensitizer Ce6 and the ferritin-targeting peptide HKN3 into the calix[4]arene composite to specifically ablate SnCs (Fig. 1). Upon being administered systemically, the HK-PCGC nanoparticles respond to SA-β-Gal. The galactose protecting group on the benzene ring is cleaved and enables the epoxy bond to break, which subsequently causes the molecule returning from the excited state to the baseline, releasing energy in the form of light, and thereby generating chemiluminescence (Supplementary Fig. 1). This triggers the CRET-driven Ce6 excitation and singlet oxygen release, leading to exaggerated lipid peroxidation and release of ferritin-bound iron for ferroptosis. Accordingly, treatment of HK-PCGC efficiently removed SnCs from either superficial or deeper tissues without affecting normal cells, thereby reversing senescent phenotypes and improving physical fitness in aged mice. Thus, by combining multiple technologies involving self-illuminating PDT, senescence-responsive CRET, in situ ROS amplification and endogenous iron hijacking, we have developed a ferroptosis-based senotherapy. This therapy has enhanced specificity, efficiency, and tissue penetration ability.

Results

Synthesis of HK-PC and characterization of HK-PCGC

To fabricate the ferritin-targeting multivalent nanoparticles, we first synthesized a Calix[4]Arene-based drug carrier conjugated with a ferritin-homing peptide HK3, namely HK-PEG-Calix[4]Arene or HK-PC (Fig. 2A). Specifically, DBCO-PEG-carboxyl and Calix[4]Arene were mixed and underwent esterification to yield the intermediate product, DBCO-PEG-Calix[4]Arene, which was subsequently linked with the ferritin-targeting peptide HK-N3 by click chemistry. As a result, the ^{1}H NMR spectroscopy revealed the chemical shift of Calix[4]Arene at approximately 6.5–7 ppm, corresponding to the proton peaks on the benzene rings of Calix[4]Arene. In parallel, the chemical shift of DBCO-

https://doi.org/10.1038/s41467-025-67364-6

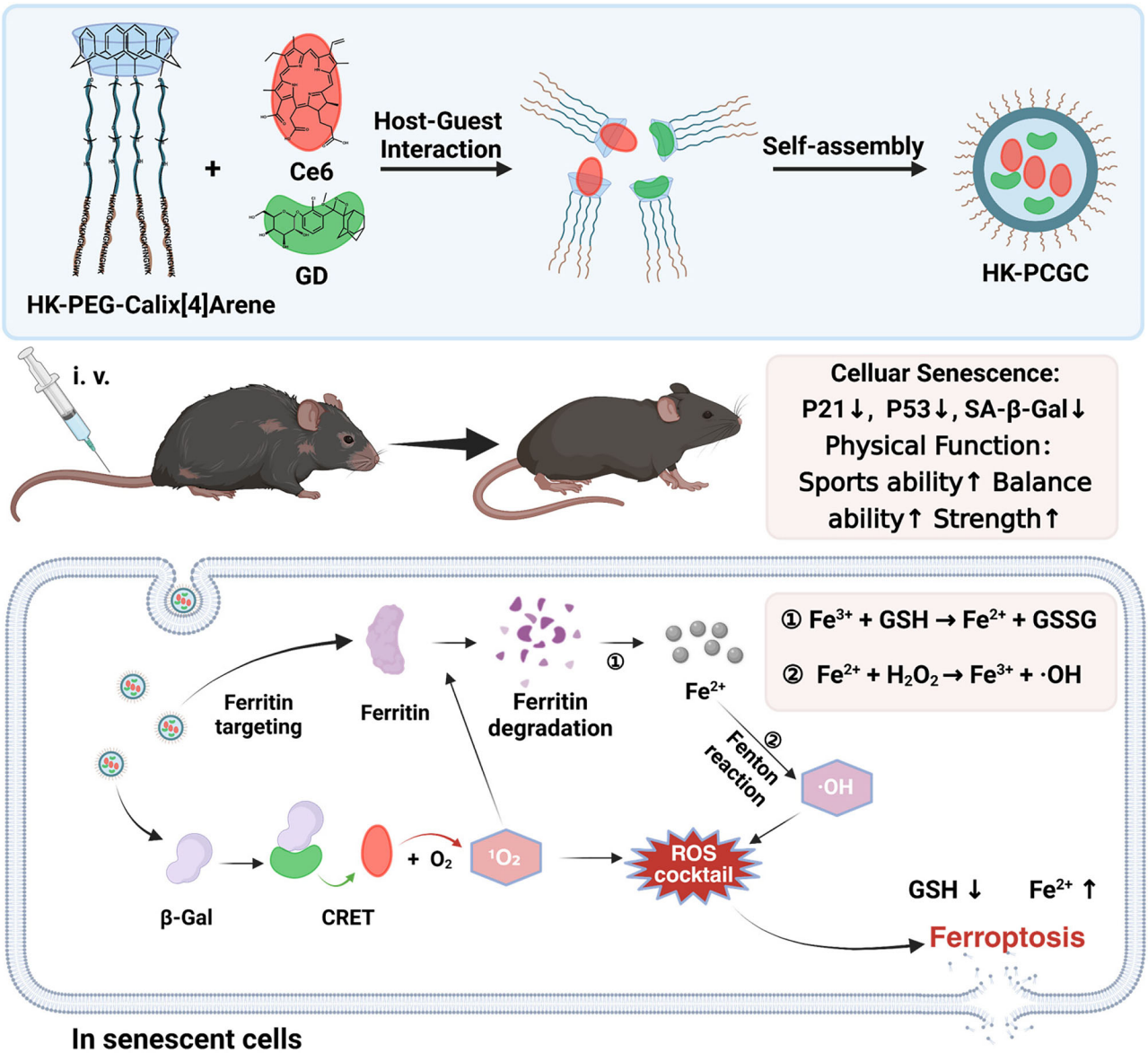

Fig. 1 | Schematic diagram of the preparation of HK-PCGC nanoparticles and the injection of the drug into aged mice to improve body function in aged mice by inducing ferroptosis to remove senescent cells (CRET: Chemiluminescence resonance energy transfer. It is a phenomenon in which the excited-state energy of a donor molecule after absorbing energy is non-radiatively transferred to an acceptor molecule). Created in BioRender. Chengkang, J. (2025) https://BioRender.com/qxtidqm.

PEG-COOH appeared at approximately 7–8 ppm (the proton peaks of the dibenzocyclooctyne), and HK-N3 was at approximately 6.5–7 ppm (the proton peaks of the benzene rings of tryptophan) (Supplementary Fig. 2). The results thus confirmed the successful synthesis of HK-PC. FTIR analysis further confirmed the successful conjugation of the HK peptide to PEG-Calix[4]arene. As evidenced, the characteristic azide absorption peak (2090–2140 cm^{-1}) disappeared in HK-PEG-Calix[4]Arene. Concurrently, a peak appears at 1400–1500 cm^{-1}, corresponding to the C=N vibration of the triazole ring formed. The polyethylene glycol segment remained unchanged, as evidenced by the persistent C-O vibration peak at 1000–1300 cm^{-1}. Collectively, these results demonstrated successful HK peptide anchoring. (Supplementary Fig. 3). As a control, we constructed a HK-PC analog, termed m-PEG-Calix[4]Arene or m-PC, by replacing DBCO-PEG-carboxyl with methoxy-PEG-carboxyl (Supplementary Fig. 4A), which disabled the complex to conjugate with HK via click reaction. The synthesized control complex was also confirmed by ^{1}H-NMR spectroscopy (Supplementary Fig. 5) and FTIR detection data (Supplementary Fig. 6). Moreover the success of the synthesis can also be demonstrated by analyzing the MALDI-TOF spectra of the raw materials and products (Supplementary Fig. 7 and Supplementary Fig. 8).

It has been demonstrated that calixarenes can self-assemble or assemble with guest molecules into the nanostructures following modulation by the appropriate groups. We then assessed the self-assembling capability of the polymers in water by examining the critical micelle concentration (CMC) using the pyrene fluorescence probe. The result showed that the CMC values for HK-PC NPs and m-PC NPs were 26 μg/ml and 19 μg/ml, respectively (Supplementary Fig. 9). The relatively low CMC indicated that the polymers were readily self-assembled into the nanomicelles and maintained its nanoscale forms in highly diluted body fluids before reaching the target site. As shown in Fig. 2B, the photosensitizer Ce6 and probe GD, as guests, entered the hydrophobic cavity of the host HK-PEG-Calix[4]Arene due to their hydrophobicity. Subsequently, nanoparticles HK-PCGC were formed through self-assembly. In addition, transmission electron microscopy (TEM) indicated that the prepared nanoparticles were spherical

https://doi.org/10.1038/s41467-025-67364-6

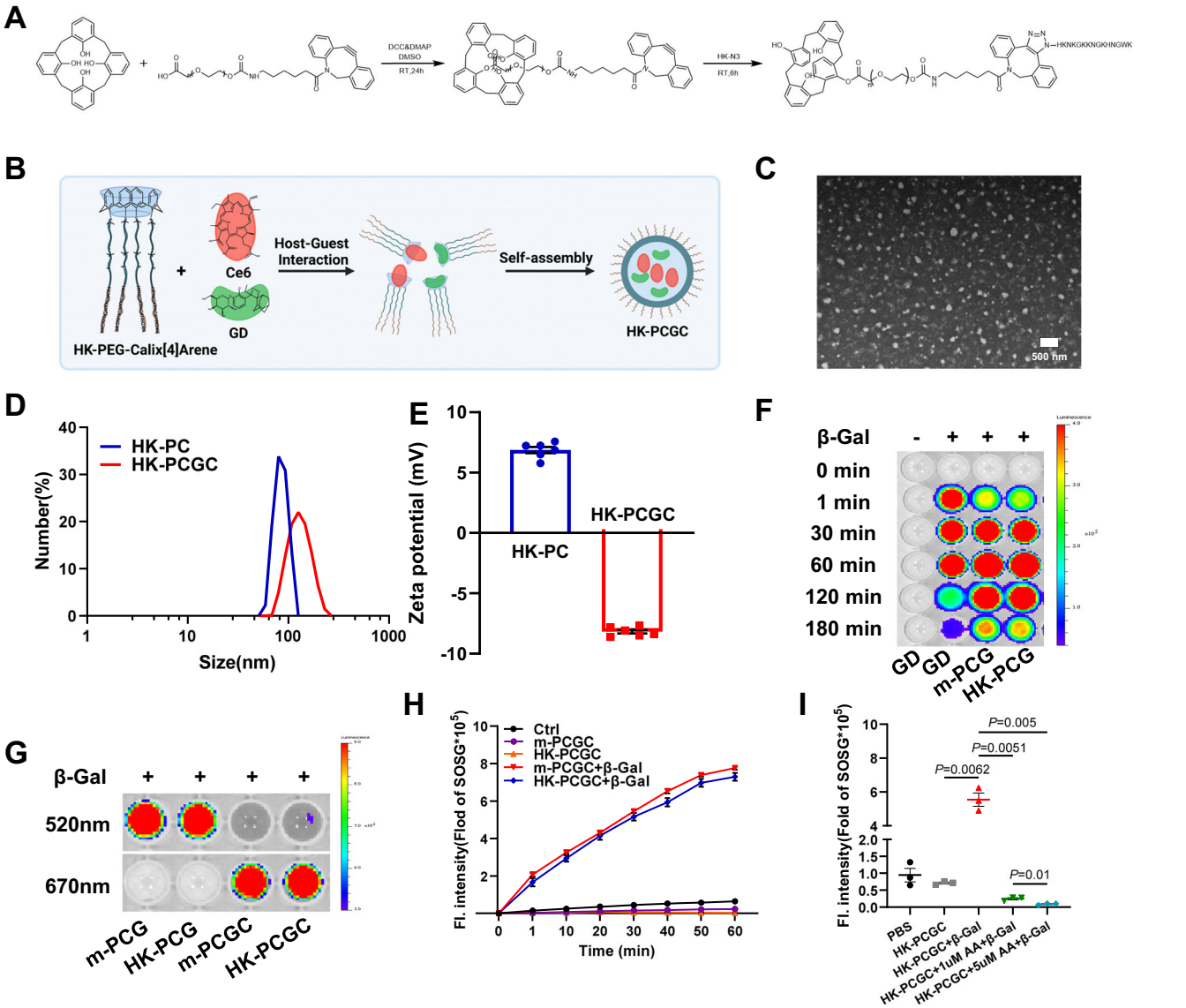

Fig. 2 | Characterization of the nanoparticles. A Synthetic route of HK-PEG-Calix[4]Arene. **B** Assembly schematic diagram of HK-PCGC NPs. Created in BioRender. Chengkang, J. (2025) https://BioRender.com/qxtidqm. **C** TEM images of HK-PEG-Calix[4]Arene NPs. Scale bar=500 nm. **D** Size distributions of HK-PC NPs and HK-PCGC NPs. **E** Zeta potential of HK-PC NPs and HK-PCGC NPs. ($n = 6$ samples, for each group). **F** Chemiluminescence kinetic imaging. **G** Chemiluminescence imaging. **H** Detection of ROS generation using an SOSG probe. m-PCGC or HK-PCGC (Ce6: 10 μM) was incubated in PBS solution containing β-galactose (5 U/mL). At the same time, PBS, m-PCGC or HK-PCGC was set as the control group. Then 5 μM of SOSG was added. The SOSG probe emits green fluorescence when reacting with singlet oxygen (λ_{ex}: 488 nm, λ_{em}: 525 nm). $n = 3$ independent experiments, in each group. **I** Detect the generation of ROS using an SOSG probe. Add ascorbic acid to quench singlet oxygen as a control ($n = 3$ independent experiments, analyze significant differences using a two-sided Student's t test, exact P values are shown in the data). Data are presented as means ± SE. Source data are provided as a Source Data file.

(Fig. 2C). Dynamic light scattering (DLS) showed that the average diameter of HK-PCGC NPs changed from 85.12 nm of HK-PC NPs to 124 nm (Fig. 2D). This is probably because when loading drugs, the hydrophobic drugs are dissolved in the hydrophobic core of the micelles. It's like filling more substances in a small space, which causes the overall volume of the micelles to increase, and thus the particle size becomes larger. In terms of zeta potential, HK-PC NPs showed a positive charge due to peptide modification, being 6.87 ± 0.26 mV, while the charge of HK-PCGC NPs was −8.17 ± 0.15 mV (Fig. 2E). Then, we compared the FTIR spectra of HK-PCGC with those of HK-PEG-Calix[4]Arene, GD, and Ce6. It was found that the peaks of HK-PCGC in the ranges of 2900–3000 cm^{-1} and 1600–1700 cm^{-1} were broader, flatter, and their intensities were significantly reduced. These changes suggest that the incorporation of GD into the hydrophobic core of HK-PEG-Calix[4]Arene may affect the vibration modes of the relevant chemical bonds[39]. Also, as shown in the fingerprint region (1300–600 cm^{-1}), the van der Waals forces altered the characteristic skeletal vibrations of the molecule. These spectral differences indicated that HK-PCGC harbored the distinct absorption characteristics relative to individual calix[4]arene, Ce6, and GD, bolstering the conclusion that HK-PCGC self-assembly was driven by the non-covalent interactions between calix[4]arene and GD/Ce6 (Supplementary Fig. 10). Furthermore, as shown in Supplementary Fig. 11A, HK-PCGC exhibited a pronounced Tyndall effect under laser irradiation compared to the water control, confirming the formation of colloidal nanoparticle upon light scattering. In parallel, Supplementary Fig. 11B demonstrated that HK-PCGC loading of GD/Ce6 yielded a homogeneous solution with no precipitation that was developed in GD+Ce6 mixtures. The observation validated the successful encapsulation of GD/Ce6 in the nanoparticles. Moreover, the results demonstrated that

the nanoparticles exhibited good stability across in a wide range of pH, supporting their reliability and feasibility in harsh TME (Supplementary Fig. 12). As a control, m-PEG-Calix[4]Arene, Ce6 and GD were self-assembled into m-PCGC NPs in the form of host-guest through self-assembly. From m-PC to m-PCGC, its particle size changed from 68.96 nm to 123.7 nm (Supplementary Fig. 4B), and the potential changed from −7.45 ± 0.33 mV to −16.40 ± 0.80 mV (Supplementary Fig. 4C).

The β-galactosidase (β-Gal) responsiveness of GD was then determined. The co-incubation of β-Gal and GD induced spontaneous fluorescence emission at the range of approximately 400-600 nm, with the peak at 470 nm (Supplementary Fig. 13A). The luminescence kinetics analysis revealed that the maximum emission of GD was at 19 min, and the half-life was 103.2 min (Supplementary Fig. 13B). The minimum limit of β-Gal detected by GD was determined as 0.08 U/ml (Supplementary Fig. 14A), confirming the high sensitivity of the glypprobe (Supplementary Fig. 14B). Notably, after encapsulating GD into m-PC or HK-PC to form m-PCG or HK-PCG, it shows an extended luminescence duration of GD in the β-Gal solution (Fig. 2F), indicating the increased stability of the glyprobe when enclosed in the calixarene nanocage. Interestingly, we noted that GD exhibited higher luminescence efficiency when encapsulated in calixarene relative to cyclodextrin, a well-defined host molecule[40] (Supplementary Fig. 15A and B), supporting the superiority of the calixarene as a PDT vector. This might be attributed to the fact that calixarenes, possessing a rigid skeleton and a preorganized cavity, can form a more intimate complex with the probes through multiple non-covalent interactions[41]. In contrast, cyclodextrins bind to the probes through a single hydrophobic interaction, and the binding energy of which is relatively low and is easily affected by the solvent polarity. Moreover, cyclodextrin complexes mostly exist as monomers and require additional crosslinking or templates to form an ordered structure, resulting in a relatively weak aggregation-enhanced effect[42]. The results thus indicated that, with the excellent responsiveness and sensitivity to SA-β-Gal, the glycoprobe facilitated the SnC-triggered activation of the nanosystem and marginally affected normal cells that generally expressed low level of β-Gal.

Next, to confirm that CRET occurs between the stimulus-responsive GD and the photosensitizer Ce6, we examined the alteration in the luminescent activity of GD upon β-Gal stimulation. Remarkably, the results showed that both m-PCGC and HK-PCGC, in response to β-Gal, exhibited a decrease in GD fluorescence emission at 470 nm concomitant with an increase in Ce6 emission at 670 nm (Fig. 2G and Supplementary Fig. 15C). Moreover, Spectral overlap between the GD chemiluminescence spectrum and the Ce6 excitation spectrum was observed (Supplementary Fig. 16), supporting efficient energy transfer. Quantification revealed a CRET efficiency (E) of 34.89% and a Förster distance (R_0) of 36 Å. Crucially, β-Gal stimulation also induced significant production of ROS by both nanosystems, as detected by the singlet oxygen sensor green (SOSG) probe (Fig. 2H). Given that ascorbic acid is a common antioxidant[43], we employed it as a control. As expected, AA treatment significantly attenuated the SOSG fluorescence signal generated by HK-PCGC upon β-Gal activation (Fig. 2I), supporting the generation of ROS in this setting. Using the SOSG probe and Ce6 as a photosensitizer, the ROS generated under these experimental conditions are likely to be singlet oxygen. The data thus indicated that Ce6, excited by β-Gal-triggered GD, elicited the fluorescence and ROS burst, laying the foundation for it to simultaneously eliminate SnCs and disrupt the ferritin shell to release iron.

Specific depletion of senescent cells by HK-PCGC NPs

We next set to study the cytotoxic effects of the nanosystems. Initially, a variety of senescent cell models were established by treating A549 cells, HepG2 cells, and NIH-3T3 cells respectively with a low level of mitomycin, a DNA alkylating agent[44]. As shown in Fig. 3A, B, 80–90% cells underwent senescence upon the induction, as detected by β-gal staining. Also, the cells demonstrated to significantly elevate the levels of p53 and p21, the hallmarks of SnCs, as compared with untreated cells (Fig. 3C). We thus successfully constructed SnCs system.

Subsequently, the effects of m-PCGC NPs and HK-PCGC NPs on senescent or non-senescent cells were evaluated (Fig. 3D-G). The results demonstrated that HK-PCGC NPs exerted the dose and time-dependent cytotoxicity to senescent but not non-senescent A549 cells. Compared with HK-functioned PCGC NPs, m-PCGC NPs displayed significantly reduced and retarded cytotoxicity to SnCs, substantiating the role of ferritin-targeting effect of HK peptide in specific killing. Then, we compared the efficiency of the ferroptosis inducer (Erastin) with that of HK-PCGC in non-senescent and senescent A549 cells respectively (Supplementary Fig. 17). The results revealed that HK-PCGC exhibited a greater selectivity toward senescent cells relative to Erastin, as evidenced by minimal cytotoxicity observed in non-senescent cells and a significantly reduced cell viability in senescent cells following treatment with HK-PCGC.

Similarly, HK-PCGC NPs depleted senescent HepG2 cells and NIH-3T3 cells in a concentration- and time-dependent manner (Figs. 3H-I and Supplementary Fig. 18), confirming the broad-spectrum cytotoxicity of HK-PCGC NPs against SnCs. Interestingly, we noted that HK-PCGC exhibited more profound effects on HepG2 cells and NIH-3T3 relative to A549 cells, correlating well with the more efficiency of senescence induction in these two cell lineages (Fig. 3B). Furthermore, the IC50 values of HK-PCGC in senescent A549, HepG2, and NIH-3T3 cells are 11.12 μM, 9.65 μM, and 5.55 μM (Supplementary Fig. 19), respectively, which appeared to be higher than IC50 of Ce6 (2.31 μM) reported in HeLa cells[45]. This might be due to altered structure and physicochemical property of the Ce6-conjucated compound. However, it should be noted that, unlike Ce6, HK-PCGC is endowed the ability to act in deeper organs with self-irradiation property. Moreover, we conducted a comparative analysis of the senescent cell clearance efficiency between HK-PCGC and the well-established senolytic drug, dasatinib (D) plus quercetin (Q). Remarkably, HK-PCGC demonstrated superior clearance efficacy to DQ, and simultaneously exhibited non-toxicity toward normal cells (Supplementary Fig. 20). To further explore this difference, we conducted the experiments and investigated the IC50 values of HK-PCGC, DQ, and Navitoclax in senescent and non-senescent cells to determine the therapeutic window. As shown in Supplementary Fig. 19A and Supplementary Fig. 21, the IC50 values of HK-PCGC in non-senescent cells and senescent cells are 76.93 μM (45.9 μg/ml) and 11.12 μM (6.63 μg/ml), respectively. In the case of DQ, IC50 values in non-senescent cells are 22.28 μg/ml, and 9.43 μg/ml in senescent cells. The IC50 values of Navitoclax in non-senescent cells and senescent cells are 14.39 μM (14.02 μg/ml) and 7.78 μM (7.68 μg/ml), respectively. These differences have successfully established a therapeutic window and fully demonstrated the specific effects of the drugs on senescent cells. Together, our data revealed that HK-PCGC NPs were able to specifically and efficiently ablate SnCs with no significant effect on non-senescent cells.

Cellular uptake and ROS generation by HK-PCGC NPs

To have a more detailed picture of HK-PCGC NPs action, we then examined the intracellular performance of the nanopolyers using confocal laser scanning microscopy (CLSM). The results demonstrated that senescent A549 cells, upon taking HK-PCGC or m-PCGC, emitted bright red fluorescence by CRET-mediated Ce6 activation. In comparison with this, non-senescent cells exhibited much weakened light emission due to lowered CRTE activation induced by the restrained β-gal activity in young cells (Fig. 4A, B). To rule out the influence of CRET luminescence on the uptake efficiency, we encapsulated Ce6 with HK-PC or m-PC to obtain HK-PCC or m-PCC. Interestingly, we found that after applying HK-PC or m-PC, the fluorescence was enhanced

https://doi.org/10.1038/s41467-025-67364-6

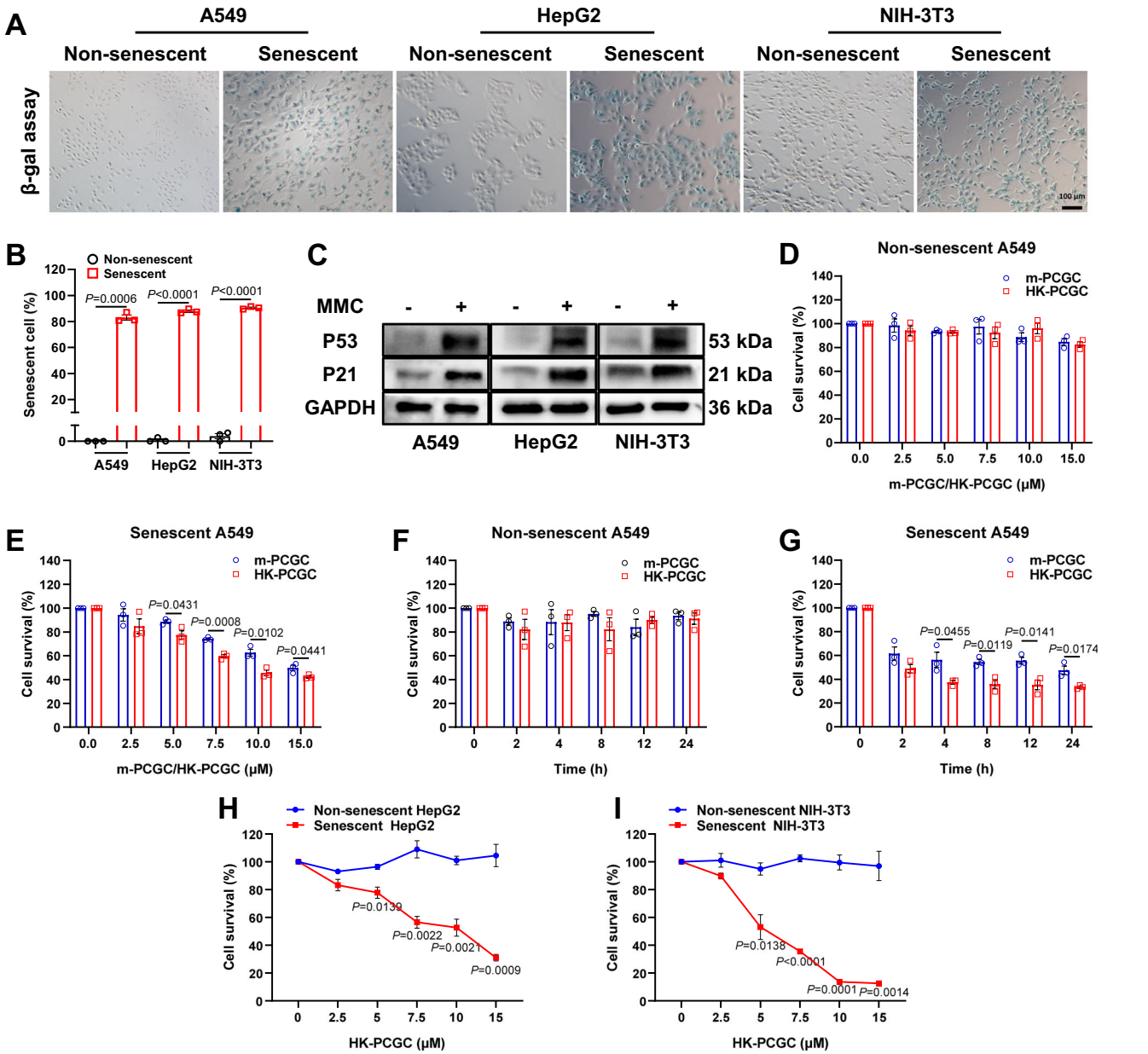

Fig. 3 | HK-PCGC kills senescent cells. A X-gal staining of senescence cells and non-senescence cells for β-gal expression. scale bar: 100 μm. **B** Statistics on the proportion of senescent cells from Figure A ($n = 3$ independent experiments in each group). For all statistical significance indications: A549: $P = 0.0006$, HepG2: $P < 0.0001$, NIH-3T3: $P < 0.0001$. **C** Western blot of p53 and p21 in normal cells and mitomycin-induced senescent cells. **D** Cytotoxicity assay of HK-PCGC and m-PCGC in different concentration on A549 cells. **E** Cytotoxicity assay of HK-PCGC and m-PCGC in different concentration to mitomycin-induced senescent A549 cells. **F** Cytotoxicity assay of HK-PCGC and m-PCGC in different time on A549 cells. **G** Cytotoxicity assay of HK-PCGC and m-PCGC in different time to mitomycin-induced senescent A549 cells. **H** Cytotoxicity assay of HK-PCGC in different concentration on HepG2 cells. **I** Cytotoxicity assay of HK-PCGC in different concentration on NIH-3T3 cells (For all statistical significance indications: 5 μM: $P = 0.0138$, 7.5 μM: $P < 0.0001$, 10 μM: $P = 0.0001$, 15 μM: $P = 0.0014$). Data are from three experiments and presented as means ± SE. Analyze significant differences using a two-sided Student's t test. Exact P values are shown in the data. Source data are provided as a Source Data file.

compared with free Ce6, which supports that the supramolecular nanoparticles fabricated in our study can enhance activity. Flow cytometry (FCM) analysis further confirmed these observations (Fig. 4C and Supplementary Fig. 22).

The results indicated that NPs were effectively taken up and predominantly localized in the cytoplasm. We next investigated the mechanism by which NPs were taken up by target cells. Initially, we observed that uptake of NPs were substantially reduced upon pre-incubation at 4 °C, indicating that the NPs internalization was an energy-driven endocytosis. Next, various endocytosis inhibitors including filipin (an inhibitor for caveolae-mediated pathway), amiloride (a macropinocytosis inhibitor), chlorpromazine (CPZ, an inhibitor for clathrin-mediated pathway), and M-β-CD (a disruptor of lipid raft), were employed to further elucidate the mechanism involved. Critically, the results demonstrated that, among the inhibitors, filipin exhibited the most pronounced effect in the reduction of NPs internalization, implying that the internalization of the nanoparticles was primarily through caveolae-dependent endocytosis. Treatment of cells with CPZ and M-β-CD also affected the internalizaiton of NPs, albeit with relatively weaker effects, suggesting the involvement of the clathrin- and lipid raft-mediated pathways in this process (Fig. 4D, E).

https://doi.org/10.1038/s41467-025-67364-6

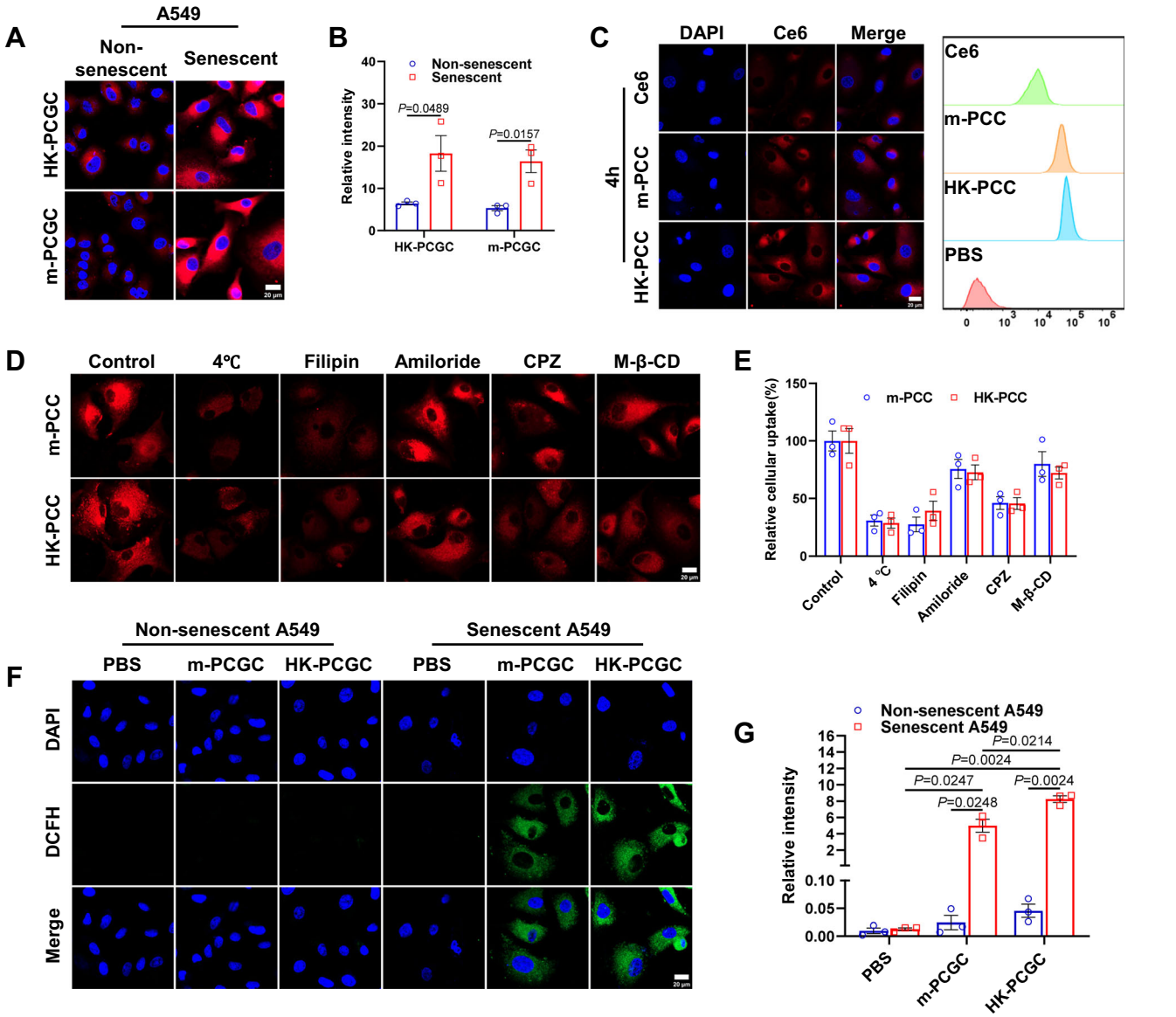

Fig. 4 | Cellular uptake and ROS generation. A Confocal fluorescence images of HK-PCGC and m-PCGC in different cells. scale bars: 20 μm, including non-senescent A549 cells and mitomycin-induced senescent A549 cells. **B** Normalized fluorescence intensity of the cells incubated with HK-PCGC and m-PCGC from parallel images including those shown in (**A**). **C** CLSM images of A549 cells exposed to free Ce6, HK-PCC NPs and m-PCC NPs for 4 h. Scale bar: 20 μm. And FCM analysis of internalization after 4 h incubation. **D** Fluorescence images of the uptake in A549 cells after treatment with different uptake inhibitors (Pre-treated for 1 h with chlorpromazine:25 μM, filipin:50 μM, amiloride:50 μM, or M-β-cyclodextrin:10 μg/ml, or alternatively, cells were incubated at 4 °C for 1 h). Scale bar: 20 μm. **E** Fluorescence quantification of the uptake from parallel images in (**D**). **F** CLSM observation of ROS generation with a DCFH-DA probe (green) of the PBS, HK-PCGC NPs and m-PCGC NPs groups in non-senescent A549 cells and mitomycin-induced senescent A549 cells. Scale bar: 20 μm. **G** Fluorescence quantification of ROS generation from parallel images in (**F**). Data are from three experiments and presented as means ± SE. Analyze significant differences using a two-sided Student's *t* test. Exact *P* values are shown in the data. Source data are provided as a Source Data file.

Since the generation of ROS by the photosensitizer is the major mechanism underlying the efficacy of PDT, we then detected ROS levels in cells following taking the nanoparticles. By exploiting 2,7-dichlorofluorescin diacetate (DCFH-DA), a cell-permeable fluorescent probe for ROS sensing, we showed that senescent but not young A549 cells generated a high level of ROS following endocytosis of PCGC NPs, with HK-PCGC NPs exerting a more profound effect than m-PCGC NPs (Fig. 4F, G).

The HK-PCGC nanoparticles in our system drive two distinct pathways in response to β-gal to promote the generation of (1) singlet oxygen ($^1O_2$) via CRET-mediated Ce6 excitation, and (2) hydroxyl radical (•OH) through ferroptosis-induced iron release from ferritin. Therefore, we then verified the •OH generation by staining with hydroxyphenyl fluorescein at cellular level. As shown in Supplementary Fig. 23, HK-PCGC-treated cells exhibited significantly enhanced fluorescence intensity relative to non-treated or m-PCG-treated control, confirming the rapid induction of hydroxyl radicals by HK-PCGC.

Given the pivotal role of ferritin in •OH generation, we next investigated whether elevating ferritin content would potentiate ROS production upon HK-PCGC treatment. We supplemented cultures with ferrous sulfate ($FeSO_4$), an iron donor can upregulate cellular ferritin content in A549 cells. As expected, according to the results shown in Supplementary Fig. 24, the amount of the produced ROS shows a significant upward trend as the concentration of $FeSO_4$ increases. More importantly, it is shown that HK-PCGC induced significantly increased levels of ROS than m-PCGC under the same concentration of

https://doi.org/10.1038/s41467-025-67364-6

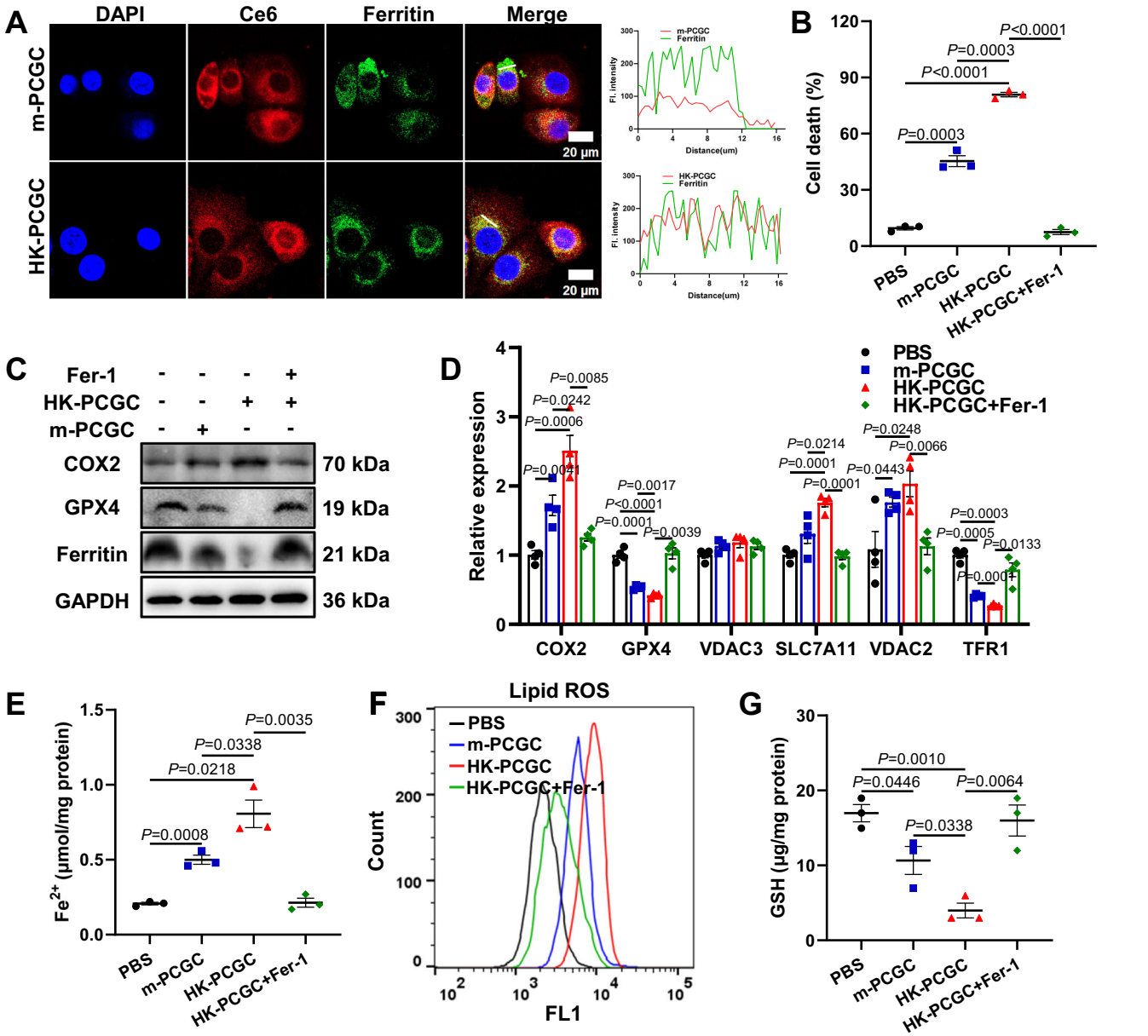

Fig. 5 | HK-PCGC kills senescent cells through ferroptosis. A The intracellular location of m-PCGC NPs, HK-PCGC NPs, and ferritin by CLSM imaging. Rabbit anti-ferritin monoclonal antibody (1:100, Abcam) was used followed by an Alexa Fluor488 goat anti-rabbit secondary antibody to mark intracellular ferritin. Scale bar: 20 μm. And plot profile for co-localization analysis of m-PCGC NPs or HK-PCGC NPs with ferritin. **B** Mortality of senescent A549 cells induced by mitomycin converted from LDH release under different treatment groups. The induction of ferroptosis by nanoparticles was detected by adding or not adding 1 μM of Fer-1 (For all statistical significance indications: PBS vs m-PCGC: $P = 0.0003$, PBS vs HK-PCGC: $P < 0.0001$, m-PCGC vs HK-PCGC: $P = 0.0003$, HK-PCGC vs HK-PCGC+Fer-1: $P < 0.0001$). **C** After incubating senescent A549 cells with m-PCGC NPs, HK-PCGC NPs, or HK-PCGC NPs + Fer-1 (Ce6: 10 μM; Fer-1, 1 μM) for 24 h. Western blot analysis of COX2 expression, GPX4 expression and Ferritin expression. **D** Expression of ferroptosis-related genes by RT-qPCR ($n = 4$ independent experiments). **E** Detection of free ferrous ion content in cells under different treatment groups. **F** Flow cytometry detection of lipid peroxidation in cells under different treatment groups. **G** Detection of GSH content in cells under different treatment groups. Data are from three experiments and presented as means ± SE. Analyze significant differences using a two-sided Student's t-test. Exact P values are shown in the data. Source data are provided as a Source Data file.

FeSO4, supporting the requirement of ferritin in the HK peptide-induced ROS generation, as previously proposed.

In support, the administration of aged mice with HK-PCGC NPs led to a greatly enhanced ROS staining in aged tissues including the liver, lungs and kidneys, whereas the tissues from young mice exhibited little ROS generation (Supplementary Fig. 25). Taken together, our data indicated that the fabricated PCGC NPs were efficiently and specifically taken by senescent cells, triggering Ce6 to generate fluorescence and a large quantity of ROS to mediate subsequent regulatory effects.

HK-PCGC promotes senescent cell ferroptosis via ferritin-disrupting ability

In our system, the PCGC NPs were designed to function with ferritin-homing peptide, HK3, to enable their migration to the iron-storing protein when internalized. To confirm it, we then examined whether Ce6-containing PCGC NPs were specifically co-localized with ferritin in SnCs. Indeed, the confocal analysis revealed a dominant overlay between ferritin (labeled by Alexa Fluor® 488) and HK-PCGC, which was indicated by red fluorescent-emitting Ce6 via CRET. By contrast, senescent A549 cells treated with m-PCGC NPs demonstrated a

substantial reduction in ferritin/Ce6 co-localization due to the lack of ferritin-targeting capability (Fig. 5A). Subsequently, we have repeated the co-localization experiments in two independent biological replicates, followed by quantitative analysis of the colocalization between the red (nanoparticle) and green (ferritin) fluorescence signals at ferritin-expressing regions. The analysis was performed on a statistically relevant number of cells ($n = 12$ per group), and the absolute Pearson coefficients were applied for statistical comparison. The results demonstrated a significantly increased colocalization of HK-PCGC with ferritin compared with that of m-PCGC and ferritin, supporting the ferritin-targeting property of HK peptide (Supplementary Fig. 26). The results thus corroborated the ferritin-homing activity of HK-PCGC NPs. Interestingly, our data showed that ferritin protein was markedly induced in senescent cells as well as aged mice tissues, thus laying the basis for ferritin-targeting therapy by HK-PCGC NPs (Supplementary Fig. 27A-D).

Since the CRET-triggered generation of ROS proximal ferritin may cause disruption of the iron-storing protein shell and release of bioactive iron to initiate the ferroptotic pathway, we thus further examined the effect of HK-PCGC NPs on the viability of SnCs. Critically, the results showed that, compared with m-PCGC NPs, HK-PCGC NPs induced a greater increase in the death of senescent A549 cells, which, however, was almost completely abrogated upon treatment with ferrostatin-1 (Fer-1), a selective inhibitor of ferroptosis (Fig. 5B and Supplementary Fig. 27E). The data thus indicated a specific induction of ferroptosis of SnCs by HK-PCGC NPs.

To determine the role of ferritin, we administered iron chelator deferoxamine (DFO). The results showed that the DFO treatment markedly mitigated the cytotoxic effects of HK-PCGC, reducing its efficacy to the level comparable to that observed in the m-PCGC control group. The data thus supported the involvement of the ferritin-mediated pathway in the mechanism of action of HK-PCGC (Supplementary Fig. 28). Notably, Ferrostatin-1 (Fer-1) treatment in m-PCGC groups exerted mild effects on cell death of senescent cells (Supplementary Fig. 29A). As can be observed, ferrostatin inhibited a portion of the cell death induced by m-PCGC, whereas it almost completely inhibited the cell death caused by HK-PCGC (Supplementary Fig. 29B). Even though both types of cell death were suppressed by ferrostatin, ferroptosis appears to be the primary killing mechanism in HK-PCGC. Taken together, these results indicate that the cell death induced by HK-PCGC is related to the release of iron ions mediated by ferritin.

In line with this, the protein level of the ferroptosis marker, Cox-2 was upregulated, while the expression GPX4, a best-characterized ferroptosis inhibitor, was significantly repressed by treatment of HK-PCGC NPs (Fig. 5C and Supplementary Fig. 30). Likewise, the expression of pro-ferroptosis genes *VDAC2*, *VDAC3*, and *SLC7A11* was elevated and that of anti-ferroptosis was decreased in SnCs treated with HK-PCGC (Fig. 5D). The observed regulatory function of HK-PCGC NPs, however, was largely abolished upon blocking the ferroptotic pathway by Fer-1, further substantiating the ferroptosis-inducing activity of HK-PCGC in SnCs.

As the disrupted ferritin would promote the release of Fe^{3+} and enable it to be converted into bioactive Fe^{2+} by intracellular reducing factors, we therefore further examined the effect of HK-PCGC NPs on liable iron concentration. The results showed that HK-PCGC NPs significantly elevated the intracellular levels of liable Fe^{2+}, and the effect was largely abrogated by Fer-1 treatment likely due to its ROS scavenging activity (Fig. 5E).

Lipid peroxidation (LPO) has been identified as the executor of ferroptotic program. In agreement, our data showed that LPO levels in senescent A549 cells were remarkably induced by HK-PCGC NPs, as detected by BODIPY 581/591 C11, a ratiometric fluorescent sensor for LPO (Fig. 5F). Depletion of lipid ROS by Fer-1 significantly compromised this effect. The level of GSH, the reducing substrate of GPx4 and hence the inhibitor of ferroptosis was consistently decreased by HK-PCGC NPs and resumed upon Fer-1 addition (Fig. 5G). Collectively, the results consistently supported that HK-PCGC hijacked intracellular ferritin and excessive LPO to induce cellular ferroptosis for depleting SnCs.

In vivo biodistribution of HK-PCGC

As the β-Gal-responsive GD probe emitted the fluorophores and excited Ce6 via CRET to release red light, we then utilized this mechanism to trace the in vivo biodistrubtion of the nanoparticles. For this, HK-PCGC NPs and m-PCGC NPs were intravenously injected into 2-month-old young mice and 18-month-old aged mice, respectively. Consequentially, the living imaging system revealed that aged mice demonstrated much stronger and sustained fluorescence in response to higher β-gal activity, when compared with their young counterparts (Fig. 6A). The semi-quantitative analysis of aged mice revealed a rapid increase in fluorescence density at early 4 h post nanoparticles instillation, followed by a gradual decline later (Fig. 6B). In comparison, the fluorescence signals in young animals were shown to fade more readily.

Furthermore, the imaging analysis demonstrated that the β-gal-elicited reaction occurred dominantly at the liver, the lung and the kidney in aged mice (Fig. 6C, D), in line with the recent report about the enrichment of SnCs in these organs of old mice[46]. Thus, the results indicated the senescence-sensing ability and superior biocompatibility of PCGC NPs, allowing the on-site activation of these senolytics to exert both monitoring and treating functions.

To further explore whether HK-PCGC is a selective tracer for in vivo aging, an induced aging model was established using 8-week-old C57/BL6 mice that were treated with a sublethal dose of doxorubicin (2 mg/kg/week, intraperitoneally) for 4 weeks. The senolytic combination DQ (D: 0.7 mg/kg, Q: 2.6 mg/kg) was administered at a 2-day intravenous course. 4 weeks later, all groups of mice, including control, doxorubicin-only, and doxorubicin-DQ-treated mice were administered with HK-PCGC nanoparticles. Expectedly, the fluorescence intensity of major organs (heart, liver, spleen, lungs, kidneys) was elevated in the doxorubicin-induced aging mice compared to controls, which was markedly reduced upon DQ treatment.

In support of the senescence-tracing effect of nanoparticles, the levels of aging markers, as exemplified by p21 and p53, were parallelly elevated in aged mice but suppressed upon DQ treatment. The gain- and loss-of-senescence observations supported our interpretation that the increased HK-PCGC signals reflected senescence burden rather than general age-related physiological changes (Fig. 6E-I).

HK-PCGC NPs removes senescent cells and attenuates SASP by in aged mice

Inspired by the specific and efficient ablation of SnCs observed above, we subsequently examined the senolytic effects of HK-PCGC NPs using naturally aged mice. To this end, 18-month-old C57BL/6 mice were intravenously instilled, twice biweekly, with HK-PCGC NPs or m-PCGC NPs (equivalent Ce6 dose of 5 mg/kg), with the canonical senolytic drug, dasatinib and quercetin (D: 0.7 mg/kg, Q: 2.6 mg/kg)[5,47], as a positive control (Fig. 7A). 8 weeks later, the data showed that both nanoparticles and DQ reduced the numbers of SA-β-gal positive cells in major organs involving the liver, lung, and kidney in aged mice, with HK-PCGC NPs exerting the effects superior to m-PCGC NPs but comparable to DQ (Fig. 7B-E).

TUNEL staining revealed that HK-PCGC NPs exhibited increased efficacy in depletion of SnCs from the aged tissues compared with m-PCGC. Both nanoparticles exerted no significant cytotoxic effects on young mice. (Fig. 7F-H).

Next, we assessed the impact of the nanoparticles on cell cycle arrest and senescence-associated secretome phenotype (SASP), the two hallmarks of SnCs. Quantitative PCR analysis demonstrated that treatment with HK-PCGC NPs significantly decrease the expression of

https://doi.org/10.1038/s41467-025-67364-6

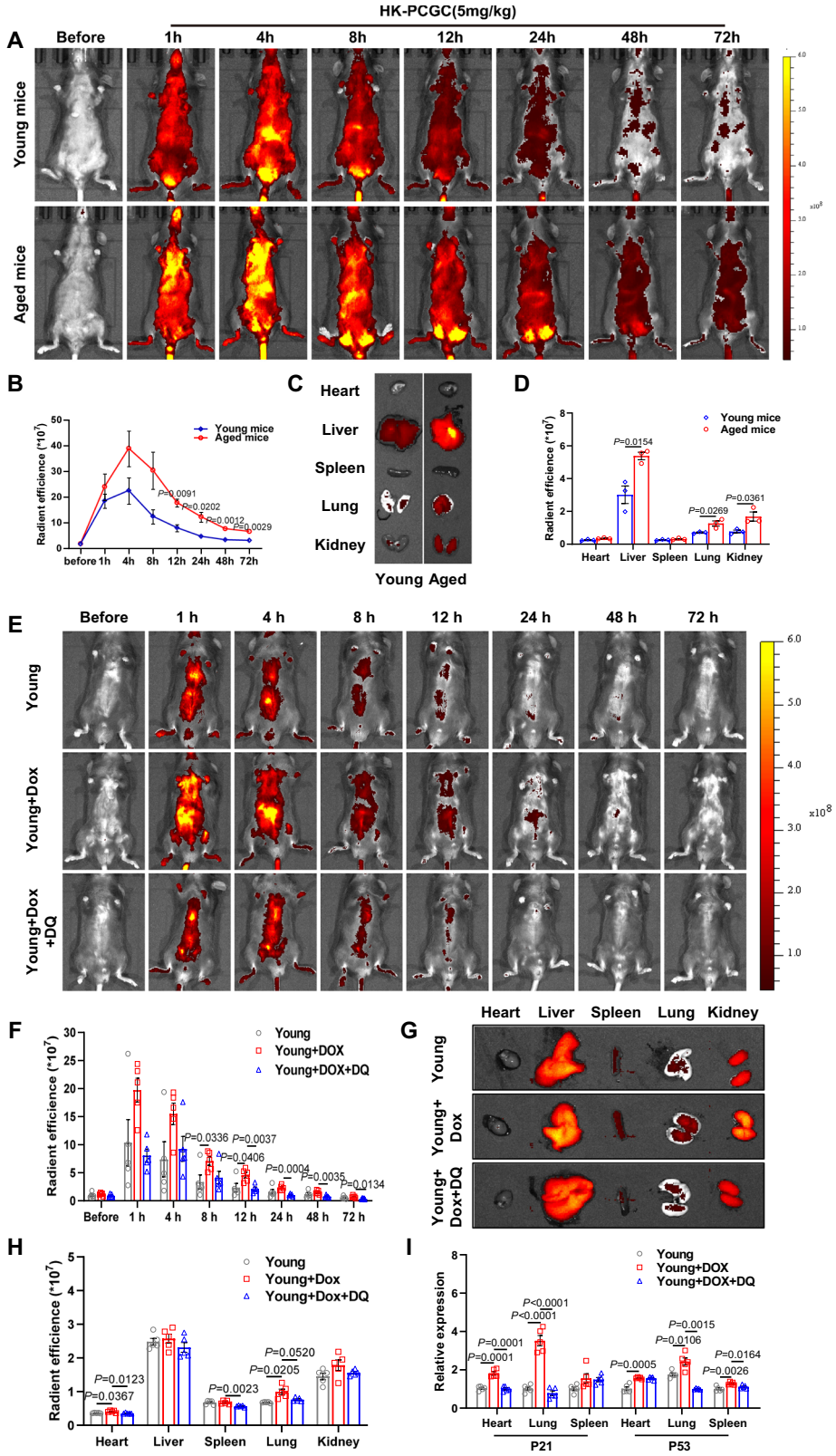

cell cycle-related genes including *p16*, *p21* and *p53*, as well as SASP-related genes such as *IL-6*, *TNF-α* and *MMP3* in aged tissues such as the liver, lung, and kidney. (Fig. 7I-K). The immunoblotting analysis also confirmed that HK-PCGC NPs significantly decreased the levels of p53 and p21, with the extent greater than m-PCGC NPs but comparable to DQ (Fig. 7L-N). Thus, our data indicated that administration of mice with HK-PCGC NPs efficiently removed the β-gal positive SnCs, reduced SASP abundance and supressed the aging-related markers in aged mice.

We further evaluate the impact of the nanosenolytics on bone microstructural changes, an age-associated physiological parameter. Three-dimensional reconstruction revealed that HK-PCGC-treated aged mice exhibited visibly smoother and more intact trabecular bone surfaces compared to untreated controls (Fig. 8A). Quantitative

Fig. 6 | Fluorescence imaging using HK-PCGC in vivo. A Representative whole-body imaging in young mice (2 months old) and naturally aged mice (18 months old) at different times after injection of HK-PCGC. **B** Quantitative analysis of the fluorescence imaging of mice from parallel images (**A**). $n = 3$ mice. **C** Representative images of ex vivo imaging of five major organs (heart, liver, spleen, lung and kidney) harvested from young mice (2 months old) and naturally aged mice (18 months old) at 72 h after injection of the HK-PCGC. **D** Quantitative analysis of the fluorescence imaging of major organs from parallel images (**C**). $n = 3$ samples. **E** Representative whole-body imaging of young mice, senescent mice (induced by dox), and senescent treatment group (induced by dox and treated with DQ) at different times after injection of HK-PCGC. **F** Quantitative analysis of the fluorescence imaging of mice from parallel images (**E**). $n = 5$ mice. **G** Representative images of ex vivo imaging of five major organs (heart, liver, spleen, lung and kidney) harvested from young mice, senescent mice (induced by dox), and senescent treatment group (induced by dox and treated with DQ) at 72 h after injection of the HK-PCGC. **H** Quantitative analysis of the fluorescence imaging of major organs from parallel images (**G**). $n = 5$ samples. **I** Detect and analyze the RNA levels of P21 and P53 in organs with fluorescence differences from parallel images (**H**). $n = 5$ samples. Data are presented as means ± SE. Analyze significant differences using a two-sided Student's t test. Exact P values are shown in the data. Source data are provided as a Source Data file.

analysis of coronal-plane Micro-CT scans showed significant improvements in multiple bone quality metrics, including increased bone volume-to-tissue volume (BV/TV) ratio, elevated trabecular number, and reduced trabecular separation (Fig. 8B-E). These findings suggest that HK-PCGC administration not only reduces the senescent cell burden but also restores bone microarchitecture and mass in aging mice.

Transcriptomic analysis of the senolytic action of HK-PCGC NPs

To further understand the action mode of the nanoparticles administrated in aged mice, we then conducted the transcriptomic analysis of the representative tissues, the lungs and liver with or without the nanosenolytics treatment. Strikingly, the RNA-sequencing identified that 2669 differentially expressed genes (DG) were induced by HK-PCGC treatment in the aged lungs, with 1314 genes up-regulated (red) and 1355 genes down-regulated (blue). The profiling of the liver however revealed that HK-PCGC treatment only induced 522 differentially expressed genes, including 194 up-regulated genes (red) and 328 down-regulated genes (blue) (Fig. 9A). To further clarify the effects of HK-PCGC on aged mice, we performed Gene Ontology (GO) analysis (Fig. 9B). It was found that the functional differences between the control group and the treatment group were mainly concentrated in the *cell part*, *binding* and *cellular process* pathways. This provides a direction for further research on the mechanism of action of HK-PCGC. The set enrichment analysis (GSEA) confirmed the modulation of aging-associated genes (Fig. 9C), and the genes related with the inflammatory response (Fig. 9D, E) upon treatment of HK-PCGC in aged mice. Moreover, treatment with HK-PCGC led to an upregulation of ferroptosis-related genes (Fig. 9F). Consistently, the heatmapping of DGs in the lungs and liver demonstrated that HK-PCGC attenuated the expression of genes related to the inflammatory cytokines, chemokines, proteases and SASP in the lungs and liver of old mice (Fig. 9G). Together, the transcriptomic analysis further substantiated that HK-PCGC administration led to a profound suppression of the inflammatory and senescent phenotypes in aged mice.

HK-PCGC improves the physical functions of aged mice

Aging leads to the decline in physical function, and removal of SnCs prove to delay aging and improve the age-related pathologies. Given the profound effect of HK-PCGC in alleviating senescence-associated phenotypes, we then proceeded to assess its impact on physiological fitness of aged mice. To this end, aged mice that were treated with HK-PCGC NPs for 8 weeks as depicted above were collected for testing their physical activity. Firstly, the running ability of mice following 3 days of training were analyzed. As illustrated in Fig. 10A, mice treated with HK-PCGC NPs displayed much longer distance following treatment of the nanoparticles and DQ, with HK-PCGC NPs having most profound effects (Fig. 10B). Also, HK-PCGC-treated mice NPs demonstrated greatly enhanced grip strength compared with the mice with no treatment or treated with m-PCGC or DQ (Fig. 10C, D).

By using the rearing test, we showed that the frequency of mice to stand on their hind legs to explore was significantly increased upon treated with HK-PCGC NPs relative to m-PCGC or DQ (Fig. 10E, F; Supplementary Movie 1). Additionally, the balance ability of mice was examined, and the results showed that HK-PCGC-treated mice took less time to cross the balance beam compared with untreated mice or treated with m-PCGC NPs or DQ (Fig. 10G, H and Supplementary Movie 2).

Collectively, our data indicate that HK-PCGC NPs, compared with m-PCGC NPs and DQ, exhibit superior effects in improving the physiological fitness of aged mice. Notably, we observed that one in five DQ-treated mice displayed hemiplegia likely due to the associated adverse effects as reported previously[48,49]. This further underscores the biosafety of the senolytic agents when they are applied in vivo.

The evaluation of biosafety of HK-PCGC NPs

To further confirm the value of HK-PCGC NPs as a promising senolytics, we further evaluated its potential cytotoxicity in normal tissues. Critically, histological examination revealed that no significant tissue damages were induced by HK-PCGC at major organs involving the heart, liver, spleen, lungs and kidneys (Supplementary Fig. 31). Treatment of nanoparticles exerted no significant effects on liver function, as demonstrated by alanine aminotransferase (ALT) and aspartate aminotransferase (AST), the renal function, as indicated by creatinine (CR) and uric acid (UA), and the lipid metabolic factors involving triglycerides (TG) and cholesterol (TC) (Supplementary Fig. 32A). Also, complete blood count analysis revealed no significant changes in the levels of neutrophils (NEU), lymphocytes (LY), white blood cells (WBC), red blood cells (RBC), and platelets (PLT) caused by HK-PCGC NPs and other treatment (Supplementary Fig. 32B). Therefore, our data suggest that HK-PCGC NPs exhibited promising therapeutic efficiency with no significant tissue-damaging effects, making it an attractive option for senolytic therapy.

Discussion

With an accelerated growth of old population and the exponential rise of age-related diseases, the development of efficient, safe and feasible intervening measures to delay aging or reverse the aging process is eagerly needed. Selective elimination of SnCs from the aging or aged tissues, termed senotherapy, has attracted increasing attention in recent years, but their efficiency, biocompatibility, and safety are far from satisfactory. A new generation of senolytics with these obstacles removed is highly desirable[50,51].

We herein develop an innovative nanosenolytic platform, termed HK-PCGC, to specifically ablate SnCs by leveraging cellular intrinsic ferroptosis and self-illuminating PDT. Specifically, the nanosenolytics were fabricated by loading the SA-β-gal-responsive fluorescent glyprobes and the photosensitizer Ce6 into the calixarene nanocages through the host-guest reaction. The calixarene complexes were preconditioned with the ferritin-homing peptide, HK3, to direct the formed supramolecules toward ferritin upon being internalized into SnCs. This nanosystem enables SA-β-gal-triggered activation of chemiluminescence and subsequent excitation of Ce6 via CRET, leading to fluorescence emission and ROS generation that acted on ferritin to release cytotoxic iron for induction of ferroptosis. Thus, by employing multiple technologies including β-gal responsive, self-powering PDT, endogenous ferroptosis robbery and calix-based drug carrier

https://doi.org/10.1038/s41467-025-67364-6

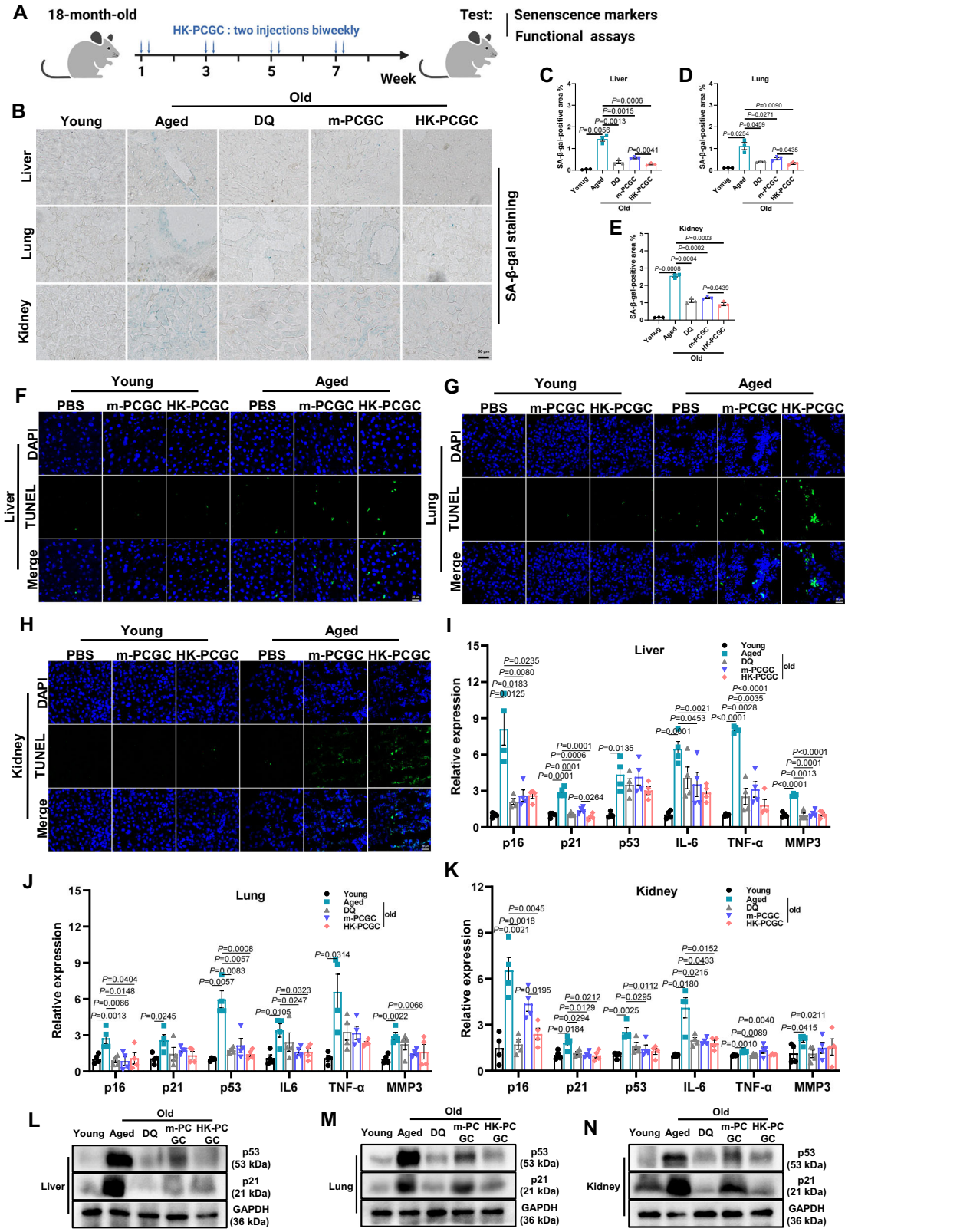

platform, we overcome the limitations associated with current senolytics to construct a nanotherapy, which potentially reduces SnCs burden at either superficial or deep tissues, and improves age-associated pathologies in naturally aging mice with marginal adverse effects. The findings extend our understanding of cell senescence and ferroptosis, opening a new avenue to develop the anti-ageing strategies with enhanced accuracy, safety and efficiency.

In this study, we devised a prodrug that utilized the "autonomous photodynamic therapy" to eliminate SnCs in a highly selective manner. This is achieved through a cascade-like reaction that is initiated by SA-β-gal-triggered chemiluminescence reaction, followed by CRET-mediated Ce6 activation. This self-powering mode bypasses the requirement of exogenous light energy input and conquers the poor tissue-penetrating ability of traditional PDT[52]. As shown in our studies,

Fig. 7 | HK-PCGC deletes senescent cells and attenuates senescence-associated signatures in aged mice. A Experimental design for HK-PCGC treatment of aged mice. For 18-month-old C57BL/6 mice, intravenous infusion was performed twice every two weeks. The mice were administered HK-PCGC nanoparticles or m-PCGC nanoparticles (equivalent Ce6 dose of 5 mg/kg). The classic senolytic drugs dasatinib and quercetin (D: 0.7 mg/kg, Q: 2.6 mg/kg) were used as positive controls. Physiological functions were detected about one week after the last administration. The mice were sacrificed after 8 weeks to detect senescence-related indicators. Created in BioRender. Chengkang, J. (2025) https://BioRender.com/ep4jnun. **B** X-gal staining of livers, lungs and kidneys for β-gal expression. Frozen tissue sections were incubated overnight in SA-β-gal staining solution at 37 °C. scale bar: 50 μm. **C** Quantification of SA-β-gal staining of livers ($n = 3$ samples). **D** Quantification of SA-β-gal staining of lungs ($n = 3$ samples). **E** Quantification of SA-β-gal staining of kidneys ($n = 3$ samples). **F** TUNEL staining of young mice and aged mice livers. Scale bar: 20 μm. **G** TUNEL staining of young mice and aged mice lungs. Scale bar: 20 μm. **H** TUNEL staining of young mice and aged mice kidneys. Scale bar: 20 μm. **F**, **G**, **H** Tissue frozen sections were subjected to TUNEL staining (green), and the nuclei were counterstained with DAPI (1:500) (blue). **I** Expression of senescence-associated genes by RT-qPCR in livers ($n = 4$ samples). **J** Expression of senescence-associated genes by RT-qPCR in lungs (n = 4 samples). **K** Expression of senescence-associated genes by RT-qPCR in kidneys ($n = 4$ samples). **L** Western blot analysis of P53 expression and P21 expression in livers. **M** Western blot analysis of P53 expression and P21 expression in lungs. **N** Western blot analysis of P53 expression and P21 expression in kidneys. Data are presented as means ± SE. Analyze significant differences using a two-sided Student's t test. Exact P values are shown in the data. Source data are provided as a Source Data file.

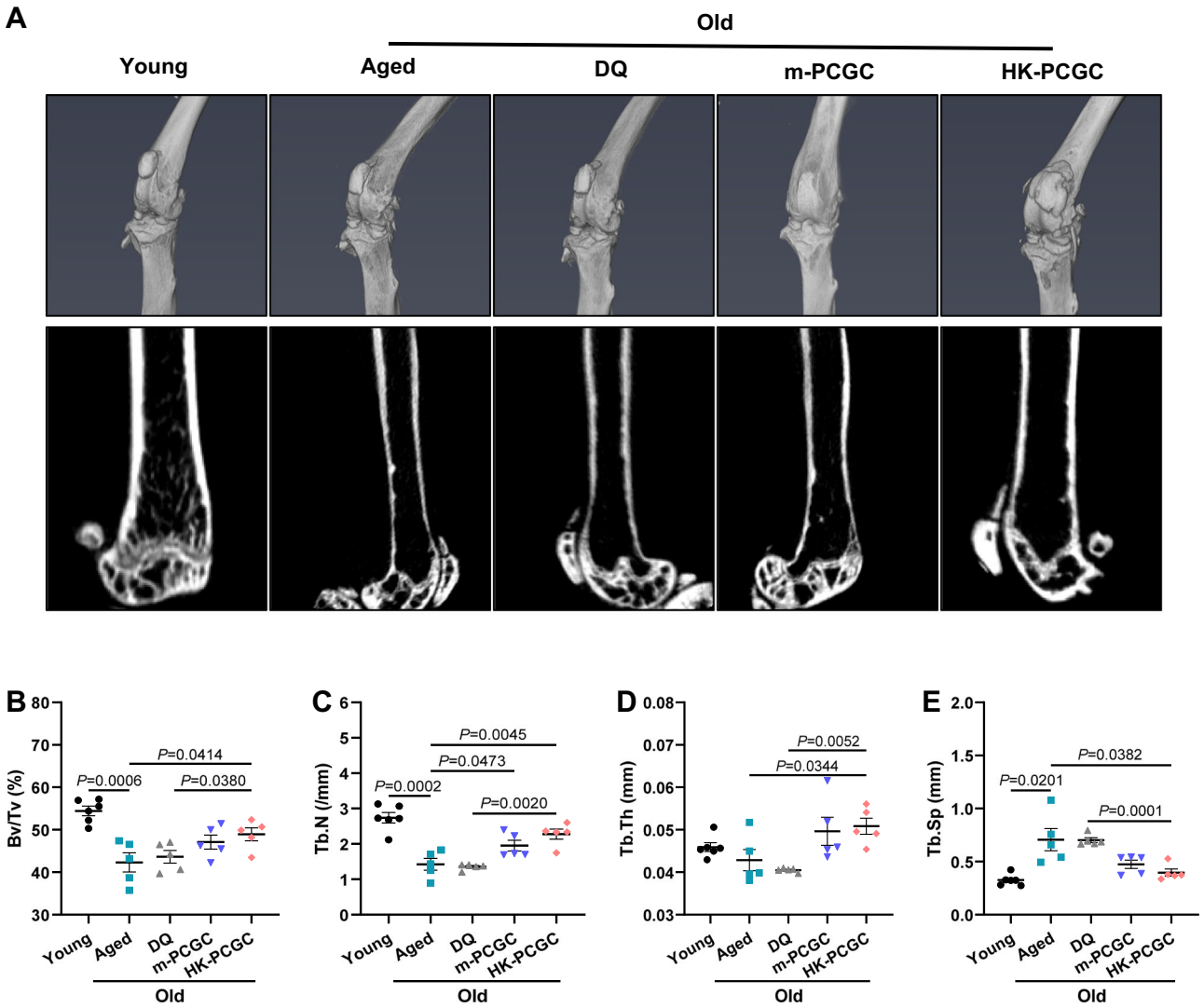

Fig. 8 | The nanosenolytic therapy on bone microstructure changes. A 3D reconstruction images of mouse knee micro-computed tomography (microCT) and coronal images of the lower end of the mouse femur. **B-E** Osteometry parameters of knee microCT ($n = 5$ samples). Bv/Tv %, Tb.N (/mm), Tb.Th (mm), Tb.Sp (mm). Data are presented as means ± SE. Analyze significant differences using a two-sided Student's t test. Exact P values are shown in the data. Source data are provided as a Source Data file.

HK-PCGC NPs efficiently purged SnCs from the aged tissues including the internally placed organs such as lungs, liver and kidneys in naturally aging mice (Fig. 6B-N). Along with the wide-spectrum cells-targeting ability, the newly fabricated nanoplatform is superior to canonical PDT requiring irradiation in order to systemically eliminate SnCs from various tissues and benefit the overall health of aged individuals [14]. Meantime, given the observation that β-gal-responsive light emission correlated well with the accumulation of senescent cells in tissues (Fig. 5A-D), our nanosystem might additionally serve to monitor in real time its therapeutic efficacy and potentially the off-target effects, in addition to its therapeutic function[53]. Thus, multiply functions including sensing, monitoring and senotherapy might be

https://doi.org/10.1038/s41467-025-67364-6

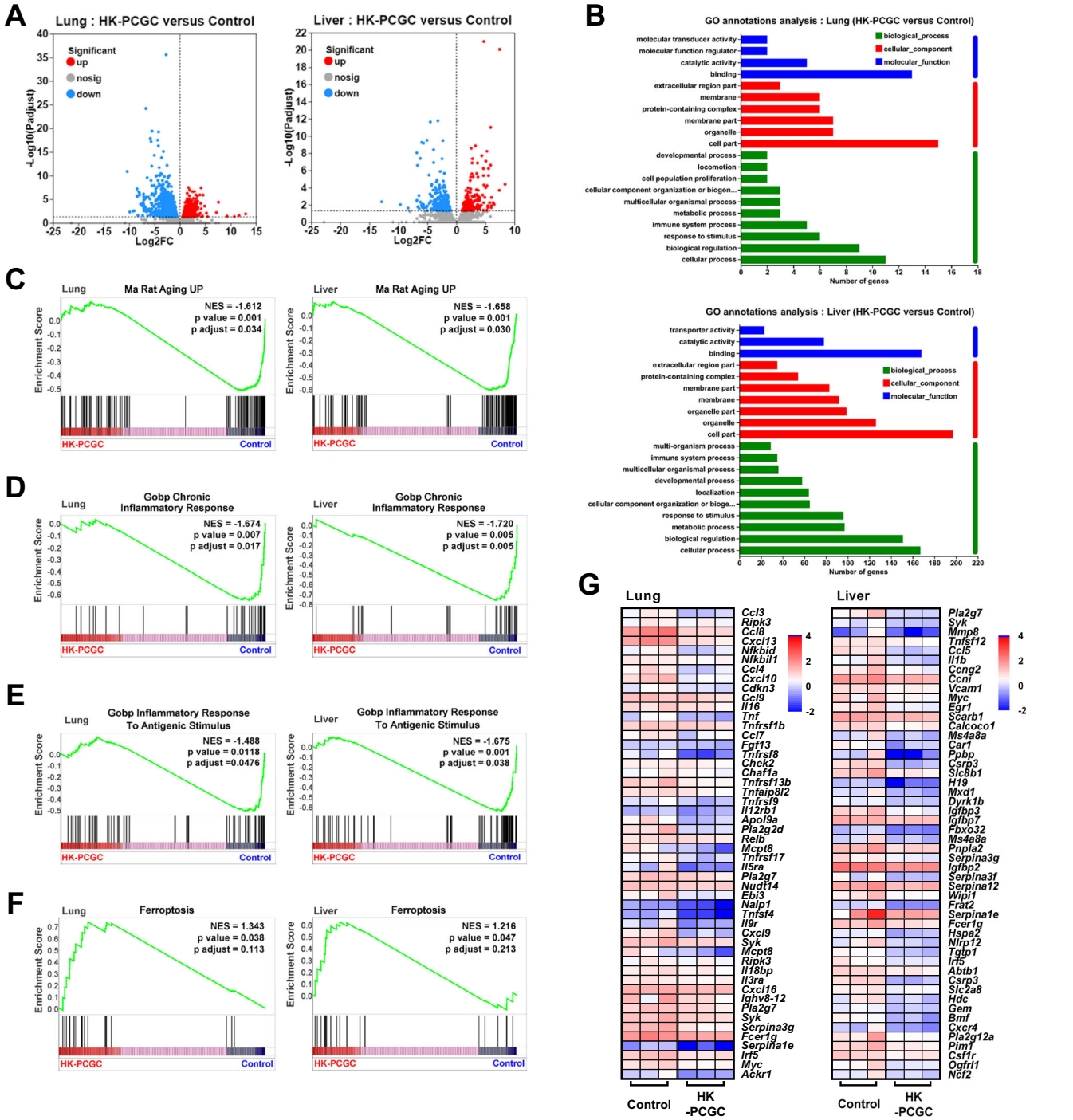

Fig. 9 | Transcriptome sequencing analysis of naturally aging mice treated with HK-PCGC. A Volcano plot analysis of total differentially expressed genes (DEGs) between HK-PCGC treatment group and aging control group. The data were analyzed on the online platform of Majorbio Cloud Platform. The analysis was performed using DESeq2. The multiple-testing corrected *P* values and the shrunken estimates of log2 fold changes were extracted from the results of the DESeq2 analysis. The significance threshold was set as: adjusted $p < 0.05$ and $|\log2FC| \geq 1$. **B** GO analysis of DEGs. **C** GSEA results of the statistically significant gene set: *Ma Rat Aging Up*. Lungs (left) and livers (right). **D** GSEA results of the statistically significant gene set: *Gobp Chronic Inflammatory Response*. Lungs (left) and livers (right). **E** GSEA results of the statistically significant gene set: *Gobp Inflammatory Response To Antigenic Stimulus*. Lungs (left) and livers (right). **F** GSEA results of the statistically significant gene set: *Gobp Inflammatory Response To Antigenic Stimulus*. Lungs (left) and livers (right). (The GSEA analyses of **C**, **D**, **E**, and **F** were conducted on the online platform of Majorbio Cloud Platform.) **G** Heat map of expression of senescence-related genes in lungs (left) and livers (right) of aging control or HK-PCGC treated.

integrated into our nanosystem, which merits further investigation to promote its translation into clinical application[54].

An ideal senolytic therapy is essentially based on the identification of core features that can differentiate normal and senescent cells. Unlike current senolytics mostly targeting the apoptotic pathway, we herein discovered a ferroptosis-based senotherapy by hijacking cellular intrinsic ferroptotic program. Despite the data from us and other investigators indicating higher levels of iron and oxidant stress, specific and efficient induction of ferroptosis of SnCs is still a challenge. Guided by the ferritin-homing peptide, our sophistically designed

https://doi.org/10.1038/s41467-025-67364-6

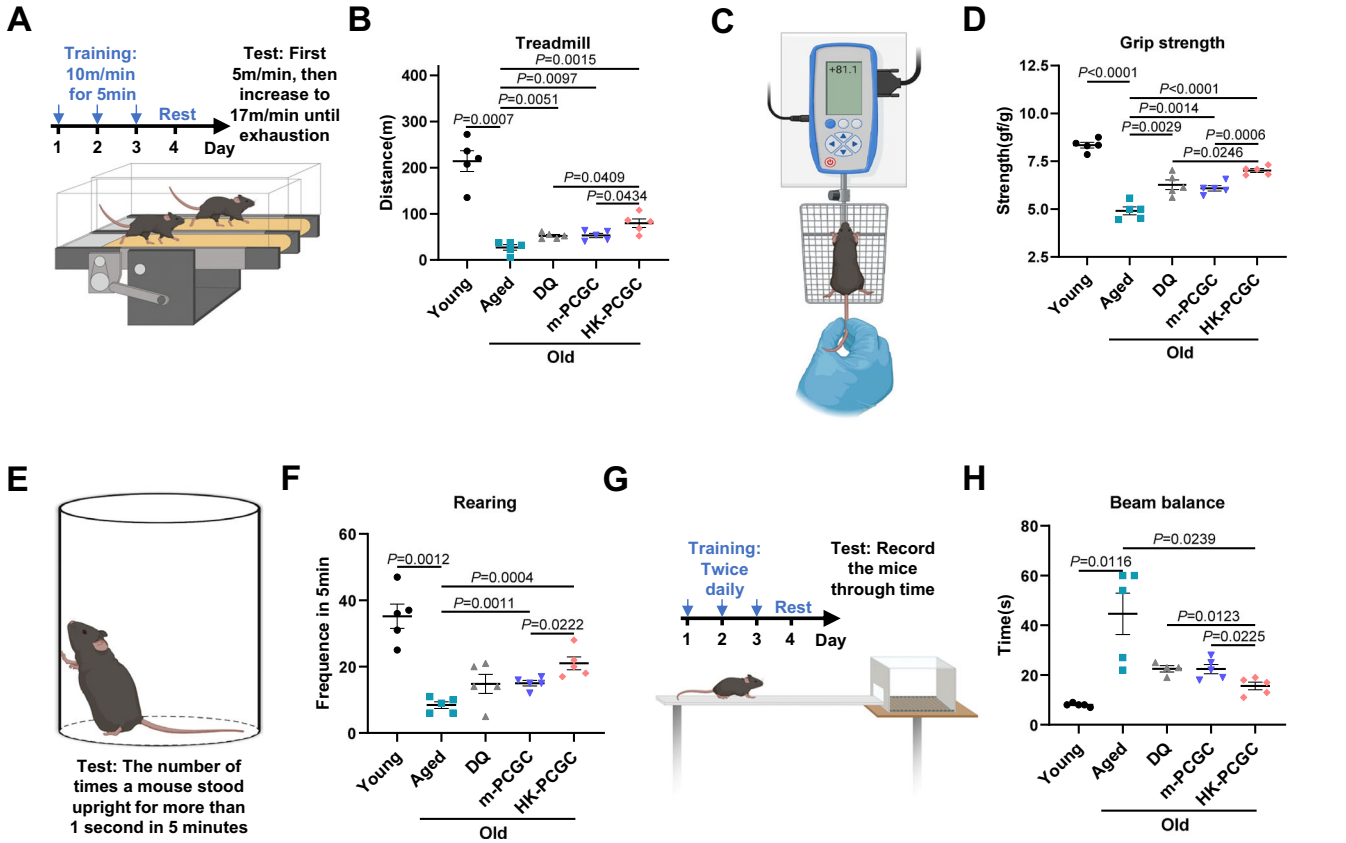

Fig. 10 | HK-PCGC improves physical function of aged mice. A Diagram of the treadmill experiment. **B** Exhaustion distance in treadmill of naturally aged mice treated with DQ, m-PCGC or HK-PCGC compared with young control, naturally aged control ($n = 5$ mice). **C** Diagram of the grip strength experiment. **D** Grip strength of four limbs of naturally aged mice treated with DQ, m-PCGC or HK-PCGC compared with young control, naturally aged control ($n = 5$ mice). For all statistical significance indications: Young vs Aged: $P < 0.0001$, Aged vs DQ: $P = 0.0029$, Aged vs m-PCGC: $P = 0.0014$, Aged vs HK-PCGC: $P < 0.0001$, DQ vs HK-PCGC: $P = 0.0246$, m-PCGC vs HK-PCGC: $P = 0.0006$. **E** Diagram of the rearing experiment. **F** The number of rearing exploration times within 5 min of naturally aged mice treated with DQ, m-PCGC or HK-PCGC compared with young control, naturally aged control ($n = 5$ mice). **G** Diagram of the beam balance experiment. **H** Time to cross balance beam for naturally aged mice treated with DQ, m-PCGC or HK-PCGC compared with young control, naturally aged control ($n = 5$ mice). Data are presented as means ± SE. Analyze significant differences using a two-sided Student's *t* test. Exact *P* values are shown in the data. Source data are provided as a Source Data file. (**A**, **C**, **E**, **G** are Created in BioRender. Chengkang, J. (2025) https://BioRender.com/u94b8ji).

nanosenolytics migrated proximately to ferritin to induce ferrophagy and Fe^{2+} release under β-gal-responsive ROS generation. The released Fe^{2+} and $^1O_2$ subsequently induced ferroptosis through the Fenton reaction. Specific induction of ferroptosis and hence depletion of SnCs are safeguarded by two mechanisms, SnC-responsive chemiluminescent reaction and ferritin-homing activity of HK peptide. As a proof-of-concept evidence, m-PCGC NPs that were devoid of HK modification demonstrated to substantially reduce the ability to colocalize with ferritin and induce ferroptosis of SnCs, resulting in compromised efficiency to ablate SnCs and improve age-related comorbidities.

It is worthwhile to mention that the amplified generation of ROS triggered by high levels of SA-β-gal would synergize with ferroptosis to enable the self-enhanced cytotoxicity and hence eliminate SnCs with increased efficacy[55]. Supportively, our data show that, compared with DQ, the ferroptosis-based nanosenolytics, albeit at a lower dose, demonstrated boosted effects in improving age-associated defective activities including muscle strength, hanging endurance, locomotor activity, and motor coordination and balance. As a control, although DQ has a similar efficiency in clearing senescent cells as HK-PCGC, it shows weaker performance in improving physiological functions, which may be due to the synergy of factors such as differences in mechanism of action or targeting specificity. In addition, the data show that the treatment with HK-PCGC nanoparticles has no obvious tissue damage effect. However, among the five mice receiving DQ treatment, one was found to have symptoms similar to hemiplegia, but there is no difference in toxic and side effects between the two. The occurrence of hemiplegia is mostly due to the production of substances toxic to the nervous system. The possible side effects[9,56,57] of DQ may lead to hemiplegia in mice through unknown pathways, and these differences cannot be detected by conventional toxicity and side effect detection.

The aging process impinges on the transcriptomic profiles of various tissues, with most profound impacts on genes related to stress, inflammation and matrix catabolism, etc. By comparing differentially expressed genes (DEGs) modulated by HK-PCGC NPs treatment, we discovered that application of the nanosystem, though having tissue-specific effects on lungs and livers, commonly down-regulated the genes enriched in the inflammation, cell death, oxidant stress and cell senescence pathways, correlating well with TUNEL and SASP results, These findings are in line with recent reports of the mechanism of canonical senolytics involving DQ[47,58,59] and further support the senescence-targeting function of the nanosenolytics. Collectively, our data consistently demonstrate the high selectivity and efficiency of HK-PCGC NPs in depleting SnCs and mitigating senescent signatures, making it an attractive option for senolytic therapy. The potential benefits against possible detrimental effects of this nanotherapy should be more carefully assessed in future studies. Also, further investigations are desirable to explore the therapeutic effects of HK-PCGC NPs on age-related pathologies to which SnCs contribute, such as neurodegenerative disorders, osteoarthritis, chronic pulmonary disease, etc.

In conclusion, by exploiting the self-illuminating PDT and cell intrinsic ferroptosis, we develop a nanosenolytic agent with improved efficiency, specificity, and safety, which may open an avenue for the development of a new generation of senotherapies to promote healthy aging.

Methods

Materials

Methoxy polyethylene glycol carboxyl (MW: 5000), dibenzocyclooctyne polyethylene glycol carboxyl (MW: 5000), and HK-N3 were purchased from Shanghai Top-Bio Technology Co., Ltd. Calix[4]arene. Chlorin E6 (Ce6), and β-galactosidase were obtained from Shanghai Yuanye Bio-Technology Co., Ltd. An adamantine-grafted fluorescent glycoprobe, Galacton-Plus™ was purchased from Thermo Fisher Scientific. Pyrene was purchased from Sigma-Aldrich. Recombinant Anti-Ferritin antibody (ab75973), Goat Anti-Rabbit IgG H&L (HRP) (ab205718), and Goat Anti-Mouse IgG H&L (HRP) (ab205719) were from Abcam. Glutathione Peroxidase 4/GPX4 antibody (sc-166120), GAPDH antibody (sc-365062), p21 antibody (sc-6246), and p53 antibody (sc-126) were purchased from Santa Cruz Biotechnology. COX2 antibody (Cat: 12375-1-AP) was purchased from Proteintech. 2′,7′-Dichlorodihydrofluorescein diacetate (DCFH-DA), Ferrostatin-1 (HY-100579), and BODIPY 581/591 C11 probe (HY-D1301) were obtained from MedChemExpress. The cell senescence β-galactosidase staining kit and lactate dehydrogenase cytotoxicity assay kit were purchased from Beyotime Biotechnology. The reduced glutathione (GSH) content assay kit and ferrous ion content assay kit were from Beijing Solarbio Science & Technology Co., Ltd. All chemical agents were used directly without further purification.

Synthesis of m-PEG-Calix[4]Arene nanoparticles

m-PEG-Calix[4]Arene was obtained through an esterification reaction. Briefly, m-PEG-COOH (68.3 mg), DCC (8.5 mg) and DMAP (0.5 mg) were dissolved in anhydrous DMSO (4.5 ml) and stirred in a 60 °C water bath for 30 min to activate the hydroxyl groups. Subsequently, a 0.5 ml anhydrous DMSO solution containing Calix[4]Arene (5.8 mg) was added dropwise to the above solution. The mixture was then stirred under a nitrogen atmosphere in a 60 °C water bath for 24 h. After that, 90 ml of pure water was added and mixed thoroughly, followed by centrifugation at 15,294 × *g* for 5 min to remove the precipitate. The supernatant was then transferred to a 3500 Da MWCO dialysis membrane. After three rounds of water dialysis to remove unreacted substances, the dialysate was lyophilized to obtain m-PEG-Calix[4]Arene. The polymer was confirmed by 1H NMR in DMSO-d6 and FTIR analysis.

Synthesis of HK-PEG-Calix[4]Arene nanoparticles

HK-PEG-Calix[4]Arene was prepared through the following two-step conjugation reaction. Firstly, PEG-Calix[4]Arene associates were prepared as described above, and HK-PC polymers were then constructed. Briefly, DBCO-PEG-Calix[4]Arene (28 mg) and HK-N3 (10 mg) were dissolved in 20 ml of pure water and stirred at room temperature for 6 h. The solution was then transferred to a 6000 Da MWCO dialysis membrane. After three rounds of water dialysis to remove unreacted substances, the dialysate is lyophilized to obtain HK-PEG-Calix[4]Arene. The polymer was confirmed by 1H NMR in DMSO-d6 and FTIR analysis.

Characterization of the prepared nanoparticles

The particle size distribution and zeta potential were analyzed using dynamic light scattering on a Litesizer 500 instrument (Anton-Paar, Austria). Morphological characteristics were examined via transmission electron microscopy with a JEM-1400flash microscope (JEOL, Japan). The optical absorption properties were recorded on a UV-2600 spectrophotometer (SHIMADZU, Japan), while fluorescence emission profiles were acquired using an FP 6500 spectrofluorometer (JASCO, Japan).

CMC measurement

The critical micelle concentration (CMC) of m-PEG-Calix[4]Arene and HK-PEG-Calix[4]Arene grafts was evaluated by a fluorescence method using pyrene as the hydrophobic probe. An initial aqueous dispersion was prepared by dissolving 10 mg of each graft copolymer in 10 mL of distilled water, followed by probe sonication (400 W, 20 cycles of 2 s sonication and 3 s pause) to yield a stock solution of 1 mg/mL. This stock solution was subsequently diluted to concentrations ranging from 0.005 to 1 mg/ml. Pyrene was introduced into each sample to attain a final concentration of 6 × 10^−7 mol/L. After 30 min of water bath sonication, the fluorescence emission spectra of pyrene were acquired with an excitation wavelength of 337 nm. The fluorescence intensities at 373 nm and 384 nm were measured, and the intensity ratio (I373/I384) was used to determine the CMC values of both graft copolymers.

Preparation of m-PCGC and HK-PCGC

500 μl of aqueous solution containing 1 mg/ml m-PEG-Calix[4]Arene or HK-PEG-Calix[4]Arene were prepared, and Ce6 in isopropanol and GD in DMSO at the indicated doses were then added. The solutions were then mixed thoroughly and sonicated in a water bath for 30 min to ensure that the hydrophobic Ce6 and GD completely enter the hydrophobic cavity of the host molecules to generate m-PCGC NPs or HK-PCGC NPs nanoparticles respectively.

Similarly, following the above method, when only the probe GD was loaded, it was named m-PCG and HK-PCG. And when only Ce6 was loaded, it was named m-PCC and HK-PCC.

The stability of HK-PCGC in different PH environments

HK-PCGC stability was evaluated in PBS at pH 5.5, 6.5, 7.4, and 8.5. Samples were incubated at 37 °C with continuous shaking. Aliquots were collected at 0, 1, 2, 4, 8, 24, and 48 h. Released Ce6 was quantified using fluorescence spectrophotometer against a standard calibration curve.

Detection of GD response to galactosidase

To determine the β-Gal-responsive chemiluminescence of GD, an aqueous solution containing 5 μM GD was added to a 96-well plate, followed by the addition of 5 U/ml of β-Gal. Measure the chemiluminescence spectrum from 400 nm to 650 nm in the presence or absence of β-Gal at 25 °C using a multifunctional microplate reader (chemiluminescence mode). The chemiluminescence kinetics of the probe reacting with β-Gal was measured over 3 h. the concentration dependency of GD was measured with β-Gal at the concentrations of 0, 2, 4, 8, 10, 16, 18 U/ml.

To confirm the specificity of GD, β-Gal, Catalase, Deoxyribonuclease I, Trypsin, BSA, or Lysozyme were added to the GD-containing solution, respectively, and the luminescence intensity was measured.

Alternatively, the responses of GD, HK-PCG, or m-PCG (GD, 5 μM) to β-Gal were measured respectively to determine the effect of the host polymer (PC, PEG-Calix[4]Arene) on the chemiluminescence kinetics of GD.

Examination of chemiluminescence resonance energy transfer

To verify the CRET of GD with Ce6, an aqueous solution containing GD or GD+Ce6 (GD: 5 μM, Ce6: 5 μM, with 10% DMSO) was added to a 96-well plate, followed by the addition of 5 U/ml of β-Gal. The chemiluminescence spectrum from 400 nm to 800 nm in the presence or absence of β-Gal at 25 °C using a multifunctional microplate reader (chemiluminescence mode).

To determine the effect of the host the host complexation (PC, PEG-Calix[4]Arene), the chemiluminescence densities induced by HK-PCGC or m-PCGC were examined.

Based on the data from Supplementary Fig. 15C, we measured the light intensity of Ce6 and GD, and applied the subsequent formula to calculate E, yielding a value of 34.89%.

$$E = \frac{Ce6 emits\ light intensity}{GD\ reduces the light intensity} * 100\% \quad (1)$$

From the data in Supplementary Fig. 16, we identified the central wavelength (λoverlap) of the overlap between donor emission and acceptor absorption as 485 nm, based on the following formula:

$$\lambda overlap = \frac{The\ emission\ peak\ of\ GD + The absorption\ peak\ of\ Ce6}{2} nm; \quad (2)$$

After consulting the literature, we estimated the fluorescence quantum yield (Q_D) of GD to be approximately 0.03 and noted the maximum extinction coefficient ($\epsilon \frac{max}{A}$) of Ce6 was $1.5 \times 10^5\ M^{-1}\ cm^{-1}$. Based on the formula as below, the Förster distance (R_0) was calculated at 36 Å.

$$R_0 = 21 * \left[Q_D * \epsilon \frac{max}{A} * \left(\lambda overlap^4 / 10^{13} \right) \right]^{1/6} Å \quad (3)$$

In vitro singlet oxygen generation detection

The SOSG probe (Shanghai Maokang Bio, S36002) emits green fluorescence upon reacting with singlet oxygen, with spectral characteristics fluorescein (λ_{ex}: 488 nm, λ_{em}: 525 nm). To perform the generation of singlet oxygen, m-PCGC NPs or HK-PCGC NPs (Ce6: 10 μM) was incubated in β-Gal-containing (5 U/mL) PBS solution, and 5 μM of SOSG was then added. Record the changes in green fluorescence of the SOSG probe over time using a fluorescence spectrophotometer.

The samples were divided into four groups: the blank control group, the HK-PCGC group, the HK - PCGC group with 1 μM AA, and the HK-PCGC group with 5 μM AA. These groups were incubated in PBS solution containing β-galactosidase (5 U/mL). Then, 5 μM of SOSG was added. After 30 min, the green fluorescence of the SOSG probe was recorded using a fluorescence spectrophotometer.

Cell lines

The A549 cell line (CL-0016), HepG2 cell line (CL-0103) and NIH-3T3 cell line (CL-0171) were purchased from Wuhan Pricella Biotechnology Co., Ltd. The cells used are all commercially available and have been verified as shown on their website: https://www.procell.com.cn/view/492.html, https://www.procell.com.cn/view/728.html and https://www.procell.com.cn/view/8947.html.

Establishment of senescent cell model

Senescent cells (SnCs) were constructed: A549 cells, HepG2 cells, or NIH-3T3 cells were respectively stimulated with 0.5 μM mitomycin (Aladdin Reagent Co., Ltd., D419552) for 2 days. The senescent signatures including β-gal staining, p16, p21 and p53 levels, as well as SASP analysis were examined to ensure the induction of senescence but not death of cells.

SA-β-gal staining

Cells or pre-dried frozen tissue sections were fixed at room temperature for 15 min and washed three times with PBS, followed by incubation in SA-β-gal staining solution (Beyotime Biotechnology, C0602) overnight at 37 °C. Afterwards, cells or tissue sections were washed and examined under a bright-field microscope, and the proportion of β-gal positive cells, or the β-gal positive areas in tissue sections were quantified using ImageJ software (NIH).

Western blot

Cells or frozen tissues were incubated in the lysis buffer (1% Triton X-100, 1% deoxycholate, 0.1% NaN3) containing protease inhibitor cocktail tablets (Roche Diagnostics). Equal volumes of the samples were separated by 10% SDS-polyacrylamide gel electrophoresis. The separated proteins were then transferred onto a polyvinylidene fluoride (PVDF) membrane and blocked with 5% non-fat milk. The membrane was then incubated overnight with the primary antibody at 4 °C, followed by incubation with the appropriate horseradish peroxidase-conjugated secondary antibody. Add the electrochemiluminescence (ECL) detection substrate and visualize the target bands using the ChemiDoc imaging system (Bio-Rad, USA).

The protein antibodies used in the above Western blot experiment are as follows: Recombinant Anti-Ferritin antibody (Abcam, ab75973, 1:2000), Goat Anti-Rabbit IgG H&L (HRP) (Abcam, ab205718, 1:1000), Goat Anti-Mouse IgG H&L (HRP) (Abcam, ab205719, 1:1000), Glutathione Peroxidase 4/GPX4 antibody (SCBT, sc-166120, 1:500), GAPDH antibody (SCBT, sc-365062, 1:500), p21 antibody (SCBT, sc-6246, 1:500), and p53 antibody (SCBT, sc-126, 1:500) and COX2 antibody (Proteintech, Cat: 12375-1-AP, 1:2000).

Cell viability assay

A549 cells, HepG2 cells, or NIH-3T3 cells were incubated with different concentrations of NPs for 24 h, or with nanoparticles at the defined concentration (equivalent to 10 μM of Ce6) for the indicated time periods. Cells were then collected and incubated in the serum-free medium containing 10 μl of CCK-8 (Cell Counting Kit-8, Beyotime, C0038) at 37 °C for 1 h. The absorbance at 450 nm was measured using a Multiskan SkyHigh full-wavelength microplate reader (Thermo Scientific, A51119500C).

Uptake of nanoparticles

Senescent A549 cells (1×10^5 cells per well) were treated respectively with free Ce6, m-PCC NPs, or HK-PCC NPs (equivalent Ce6 at 10 μM) for 4 h. Cells were then collected, fixed with 4% paraformaldehyde and stained with DAPI. FCM (ACEA NovoCyteTM, ACEA Biosciences, USA) was used to quantify NPs uptake, and laser confocal scanning microscopy (laserA1R, Nikon, Japan) imaging was used to characterize the distribution of NPs.

Internalization and endocytosis of nanoparticles

Senescent A549 cells were pre-treated respectively with specific inhibitors of internalization or endocytosis including chlorpromazine (25 μM), Filipin (50 μM), Amiloride (50 μM), or M-β-CD (10 μg/ml) for 1 h, and alternatively cells were incubated at 4 °C for 1 h. After that, cells were treated with m-PCC NPs or HK-PCC NPs (Ce6 concentration: 10 μM) for an additional 4 h. Fluorescence intensity of cells was then detected by CLSM and quantitatively analyzed using ImageJ software (NIH).

ROS detection by DCFH-DA

Non-senescent and senescent A549 cells were seeded in 6-well plates and subjected to a 4 h treatment with PBS, m-PCGC NPs, or HK-PCGC NPs (at a Ce6 equivalence of 10 μM). Following this incubation, the medium was replaced with fresh medium containing 20 μM DCFH-DA, and the cells were further incubated for 30 min. After trypsinization and collection, the cells were fixed and nuclei were counterstained with DAPI. Finally, intracellular DCF fluorescence was visualized immediately under a CLSM, and fluorescence intensity was quantified using ImageJ software (NIH).

·OH detection by HPF

Senescent A549 cells were plated in 6-well plates and treated for 4 h with PBS, m-PCGC nanoparticles or HK-PCGC nanoparticles (equivalent Ce6 conc.: 10 μM). The culture medium was then exchanged for one containing 10 μM hydroxyphenyl fluorescein (HPF), and incubation continued for another 30 min. Following this, the cells were harvested, fixed, and their nuclei stained with DAPI. HPF-derived fluorescence was immediately captured by CLSM, and the signal intensity was quantified using ImageJ software.

In a separate set of experiments, A549 cells were pre-incubated for 24 h with varying concentrations of ferrous sulfate (0, 10, 50, and 100 μM) prior to a 4-h exposure to HK-PCGC nanoparticles (equivalent Ce6 concentration: 10 μM). Intracellular ROS generation was evaluated based on HPF fluorescence (10 μM, 30 min incubation) as visualized by CLSM and quantified with ImageJ. In parallel, cell samples from the same treatments were subjected to western blot analysis to determine ferritin expression levels.

Colocalization of NPs with ferritin

Senescent A549 cells were incubated with m-PCGC NPs or HK-PCGC NPs (Ce6: 10 μM) for 4 h. After washing with PBS, cells were fixed with 4% paraformaldehyde and permeabilized with 0.1% Triton X-100. The intracellular ferritin was labeled with a rabbit anti-ferritin monoclonal antibody (1:100, Abcam), followed by reaction with Alexa Fluor® 488 goat anti-rabbit secondary antibody. The nuclei were stained with DAPI. The fluorescence excitation was imaged by CLSM, and the colocalization was analyzed using ImageJ software (NIH).

Determining ferroptosis by LDH cytotoxicity assay

The optimal concentration of the ferroptosis inhibitor, Fer-1 were firstly determined by LDH assay. For this, 8*10^3 senescent A549 cells were seeded and treated with HK-PCGC NPs with or without Fer-1 at the dose of 0.1, 0.5, 1, 5, 10 μM respectively. Appropriate controls were set up, including the background control with culture medium only and the maximum enzyme activity control with non-treated cells. One hour before the scheduled time, LDH reagents was added to the maximum enzyme activity control. All the cell cultures were recovered as scheduled and centrifuged at 400 *g* for 5 min. 120 μL of the supernatant was then collected, mixed with 60 μl of LDH solution, and incubated at room temperature in the dark for 30 min. The absorbance was measured at 490 nm.

Senescent A549 cells (8*10^3 cells per well) were seeded into 96-well plates. The cells were then incubated with m - PCGC nanoparticles, HK-PCGC nanoparticles, HK-PCGC nanoparticles + Fer-1 (Ce6: 10 μM; Fer-1, 1 μM), or m-PCGC nanoparticles + Fer-1 (Ce6: 10 μM; Fer-1, 1 μM) for 4 h. For each experimental group, three wells were inoculated with cells from three separate culture dishes to ensure experimental reproducibility. Subsequently, the induction of ferroptosis by the nanoparticles was detected following the previously described experimental procedure. Cell cytotoxicity (%) was calculated as follows:

$$\begin{aligned}\text{Cellcytotoxicity}(\%) = {} & (\text{Absorbance of treated sample} \\ & - \text{Absorbance of background blankcontrol})/ \\ & (\text{Absorbance of maximumenzyme activity control} \\ & - \text{Absorbance of background blank control}) \times 100\end{aligned} \tag{4}$$

Quantitative real-time PCR (qRT-PCR)

Total RNA was isolated from cell pellets or snap-frozen tissues (lung, liver, or kidney) with Trizol reagent (Thermo, USA). Following isolation, The RNA samples were reverse transcribed into cDNA employing a commercial kit (gDNA wiper, Vazyme, R22201). The resultant cDNA products were diluted 5–10 fold in DEPC-treated water and stored at −20 °C until use. Quantitative real-time quantitative PCR (qRT-PCR) analyses were carried out on an ABI Prism 7500 system (Applied Biosystems, USA) with SYBR Green Master Mix (Accurate Biology, AG11701). The relative expression levels of target genes were normalized to β-actin as an internal control and calculated via the 2−ΔΔCT method. The primers were synthesized by Beijing Qingke Biotechnology Co., Ltd. The primer information is shown in Supplementary Table 1 and Supplementary Table 2.

Determination of free iron content

Senescent A549 cells were seeded in T75 cell culture flasks (2 × 10^6 cells per flask) and cultured for 24 h, and the nano-drugs were added to the corresponding cell cultures for another 4 h. Cells were then harvested and resuspended in 1 mL PBS for subsequent analysis with dividing into two parts. Specifically, 800 μl of cell suspension was sonicated in ice bath, lysed and centrifuged to obtain the supernatants, which were then transferred to a 30 kDa ultrafiltration centrifuge tube for centrifugation at 3500 *g* for 20 min. Finally, the filtration was collected for detection of ferrous ion content as per the instructions provided with the ferrous ion detection kit (Solarbio, BC5415). The remaining 200 μl of cell suspension was centrifuged to obtain the cell pellets, which were incubated at 50 μl of RIPA lysis buffer for lysis. The lysates were then recovered after centrifugation and total protein was quantified using a BCA assay. The free ferrous ion content was expressed as the iron content per milligram of total proteins.

GSH detection

Senescent A549 cells were seeded in T75 cell culture flasks (2 × 10^6 cells per flask) and cultured for 24 h, which were then treated with nano-drugs for 4 h. After incubation, the cells were harvested and resuspended in 1 mL PBS, which were divided into two parts for subsequent analysis. Specifically, 800 μl of cell suspension underwent 2–3 cycles of freeze-thawing and then centrifuged at 12,000 *g* for 10 min. The supernatant was collected for GSH content detection. The remaining 200 μl of cell suspension was centrifuged, and cell pellets was recovered for lysis as described above. GSH content was measured according to the protocol provided by the kit (Solarbio, BC1175), and expressed as the GSH content per milligram of cellular protein.

Lipid peroxidation detection

Senescent A549 cells (1*10^5 cells per well) were seeded into 6-well plates and incubated respectively with m-PCGC NPs, HK-PCGC NPs, or HK-PCGC NPs + Fer-1 (Ce6: 10 μM; Fer, 1 μM)) for 12 h. The medium was then replaced with fresh medium containing C11-BODIPY581/591 (5 μM) and incubated for another 20 min. The fluorescence emission was then detected at Red (λ_{ex}: 581 nm, λ_{em}: 591 nm) and Green (λ_{ex}: 500 nm, λ_{em}: 510 nm) by FCM.

Mice

The present study utilized C57BL/6 (C57) mice supplied by Hangzhou Hans Biological Technology Co., Ltd. All animals were maintained under strict specific pathogen-free (SPF) conditions, with a 12-h light/dark cycle and libitum access to food and water. The experimental protocols were conducted in full compliance with guidelines and were approved by the Animal Ethical Review Committee of NJUCM (20200326).

In vivo Imaging of nanoparticles

The biodistribution of HK-PCGC or m-PCGC NPs were tracked in live mice using a PerkinElmer IVIS Spectrum CT imaging system (Ex/Em: 535 nm/640–660 nm) at 1, 4, 8, 12, 24, 48, and 72 h post injection. After the final in vivo scan, mice were sacrificed, and key organs (heart, liver, spleen, lungs, kidneys) were excised for immediate ex vivo imaging.

To evaluate the anti-aging effect, eight-week-old C57 mice were divided into three groups: Normal control, Doxorubicin-induced aging

control (doxorubicin at a dose of 2 mg/kg per week[60]), and Doxorubicin-induced aging + DQ treatment group (doxorubicin at a dose of 2 mg/kg per week; after doxorubicin injection, DQ treatment was administered by intravenous injection for two consecutive days (D: 0.7 mg/kg, Q: 2.6 mg/kg)). After four weeks of modeling and treatment, all mice received HK-PCGC nanoparticles and were imaged according to the above biodistribution protocol. Organ RNA was then extracted to assess the expression of senescence markers.

ROS detection by DHE

Frozen sections of the liver, lungs, and kidneys were prepared and subjected to DHE staining according to the manufacturer's instructions (Servicebio, G1045), with the nuclei counterstained with DAPI (1:500). Fluorescence imaging and digital slide scanning of fluorescence intensity were performed.

TUNEL staining

Frozen sections of the liver, lungs, and kidneys were subjected to TUNEL staining according to the manufacturer's instructions (Beyotime, C1086), with the nuclei counterstained with DAPI (1:500). The positive signals were imaged using CLSM.

RNA sequencing

Following RNA extraction from liver and lung tissues of the aged mice treated or untreated with HK-PCGC NPs, sequencing and raw data QC were carried out by Shanghai Majorbio Biomedical Technology Co., Ltd. The Majorbio Cloud Platform was utilized for downstream data processing, and genes meeting the criteria of $|\log_2(\text{fold change})| \geq 1$ and $p < 0.05$ were identified as differentially expressed.

Mouse-adapted gene sets were acquired via the msigdbr package (version 7.0.1, https://cran.rproject.org/web/packages/msigdbr/index.html), which facilitates the use of human MSigDB (MSigDB v7.0, http://software.broadinstitute.org/gsea/msigdb/index.jsp) collections in model organisms by mapping original human genes to their homologous counterparts.

Physical function measurements

All functional assays are conducted at least 5 days after the last administration of nanoparticles. A treadmill fatigue test was applied to evaluate the exercise capacity and endurance of mice. For this, an electric treadmill with a 5° incline and 0.5 mA electric stimulation (Shanghai Xinsoft Information Technology Co., Ltd., XR-PT-10B) were utilized. Mice were pre-trained at a speed of 10 m/min for 5 min. After three training sessions and 1 day of rest, the mice were tested by starting at a speed of 5 m/min and increasing to 17 m/min, ending at the speed the mice were unable to keep up with. Record the distance (m) each mouse walked before exhaustion.

To assess the grip strength, mice were placed on top of a grid strength meter (Shanghai Xinsoft Information Technology Co., Ltd., XR501), allowing them to grasp the grid with all four paws. Set the meter to peak tension (T-PK) mode and record the grip strength in seven trials. With exclusion of the highest and lowest values, the average grip strength (gf) were calculated and normalize by dividing with mouse's body weight (g) to obtain the weight differences.

For open field test, mice were transferred from the housing room to the testing room and allowed them to acclimate to the new environment for at least 30 min before testing. Carefully place mice in a transparent cylinder 14 cm high and 11 cm in diameter, and record mice behaviors for 5 min using a camera. Analyze the video to measure the rearing frequency, which was defined as mice standing on its hind legs with front paws off the ground for more than 1 s.

A balance beam test was conducted to assess motor balance and coordination of mice. Briefly, mice were placed on a 1-m long and 6-mm wide beam with 60 cm above the ground. A black box filled with nesting material from mice home cages was equipped at one end of the beam as a goal. Mice were trained to across the beam to the black box for 3 days, followed by one day of rest. After that, mice were placed at one end of a beam and the time required to cross to the box at the other end (80 cm away) was measured.

Histopathological examination and blood biochemistry test

Following collection, major organs were processed for histological evaluation. The tissues were fixed, dehydrated, and embedded in paraffin, after which sections were prepared and stained with H&E (hematoxylin and eosin) for microscopic examination.

Complete blood count was performed on 100 µl of fresh blood anticoagulated with EDTA, using a Celltac Alpha MEK-6400 series hematology analyzer (Nihon Kohden, MEK-6400).

Serum was obtained by allowing blood samples to clot (2 h at room temperature or overnight at 4 °C), followed by centrifugation at 1000 × g for 10 min. Serum concentrations of ALT, AST, UA, CR, TG, and TC were determined with a Mindray BS-350E clinical chemistry analyzer.

Statistical analysis

All data are presented as mean ± standard error (SE) ($n = 3$ unless otherwise stated), and the analysis was conducted using GraphPad Prism 8.0. Error bars represent the standard error (SE) derived from three independent measurements. Analyzed significant differences using a two-sided Student's t test. When performing an independent samples t-test, conducted a homogeneity of variance test first. If the variances were homogeneous, used a t-test with equal variances. If the variances were not homogeneous, used a t-test with unequal variances. For comparison of three or more groups of data, analysis of variance (ANOVA) method was used. If the results of ANOVA showed significant differences, post hoc tests (such as Tukey's test, Bonferroni test, etc.) were further used to determine which specific groups had significant differences. Exact P values were shown in the data.

Reporting summary

Further information on research design is available in the Nature Portfolio Reporting Summary linked to this article.

Data availability

All data is available within this paper or as Supplementary Information. Source data are provided with this paper. Gene expression data for RNA sequencing in mouse lung/liver tissues can be obtained through the National Center for Biotechnology Information (PRJNA1201546). The systematic names of the gene sets used in the GSEA analysis are: MM16096 [https://www.gsea-msigdb.org/gsea/msigdb/mouse/geneset/MA_RAT_AGING_UP.html], MM4302 [https://www.gsea-msigdb.org/gsea/msigdb/mouse/geneset/GOBP_CHRONIC_INFLAMMATORY_RESPONSE.html], MM4267 [https://www.gsea-msigdb.org/gsea/msigdb/mouse/geneset/GOBP_INFLAMMATORY_RESPONSE_TO_ANTIGENIC_STIMULUS.html], M39768 [https://www.gsea-msigdb.org/gsea/msigdb/geneset_page.jsp?geneSetName=WP_FERROPTOSIS&keywords=ferroptosis]. Source data are provided with this paper.

References

1. López-Otín, C., Blasco, M. A., Partridge, L., Serrano, M. & Kroemer, G. Hallmarks of aging: an expanding universe. *Cell* **186**, 243–278 (2023).
2. Guo, J. et al. Aging and aging-related diseases: from molecular mechanisms to interventions and treatments. *Signal Transduct. Target. Ther.* **7**, 391 (2022).
3. Gorgoulis, V. et al. Cellular senescence: defining a path forward. *Cell* **179**, 813–827 (2019).
4. Leeman, D. S. et al. Lysosome activation clears aggregates and enhances quiescent neural stem cell activation during aging. *Science* **359**, 1277–1283 (2018).

5. Xu, M. et al. Senolytics improve physical function and increase lifespan in old age. *Nat. Med.* **24**, 1246–1256 (2018).
6. Childs, B. G. et al. Senescent cells: an emerging target for diseases of ageing. *Nat. Rev. Drug Discov.* **16**, 718–735 (2017).
7. He, S. & Sharpless, N. E. Senescence in health and disease. *Cell* **169**, 1000–1011 (2017).
8. Hickson, L. J. et al. Senolytics decrease senescent cells in humans: preliminary report from a clinical trial of Dasatinib plus Quercetin in individuals with diabetic kidney disease. *EBioMedicine* **47**, 446–456 (2019).
9. Zhu, Y. et al. The Achilles' heel of senescent cells: from transcriptome to senolytic drugs. *Aging Cell* **14**, 644–658 (2015).
10. Chang, J. et al. Clearance of senescent cells by ABT263 rejuvenates aged hematopoietic stem cells in mice. *Nat. Med.* **22**, 78–83 (2015).
11. Fuhrmann-Stroissnigg, H. et al. Identification of HSP90 inhibitors as a novel class of senolytics. *Nat. Commun.* **8**, 422 (2017).
12. Guerrero, A. et al. Cardiac glycosides are broad-spectrum senolytics. *Nat. Metab.* **1**, 1074–1088 (2019).
13. Xu, Q. et al. The flavonoid procyanidin C1 has senotherapeutic activity and increases lifespan in mice. *Nat. Metab.* **3**, 1706–1726 (2021).
14. Rad, A. N. & Grillari, J. Current senolytics: mode of action, efficacy and limitations, and their future. *Mech. Ageing Dev.* **217**, 111888 (2024).
15. Stockwell, B. R. Ferroptosis turns 10: emerging mechanisms, physiological functions, and therapeutic applications. *Cell* **185**, 2401–2421 (2022).
16. von Krusenstiern, A. N. et al. Identification of essential sites of lipid peroxidation in ferroptosis. *Nat. Chem. Biol.* **19**, 719–730 (2023).
17. Lei L. et al. Targeting the Labile iron pool with engineered DFO nanosheets to inhibit ferroptosis for Parkinson's disease therapy. *Adv. Mater.* 36, e2409329 (2024).
18. Zhu L. et al. Ferritin-hijacking nanoparticles spatiotemporally directing endogenous ferroptosis for synergistic anticancer therapy. *Adv. Mater.* **34**, e2207174 (2022).
19. Zou, P. et al. Implanted, wireless, self-powered photodynamic therapeutic tablet synergizes with ferroptosis inducer for effective cancer treatment. *Adv. Sci.* **10**, e2302731 (2023).
20. Wang, Q. et al. Enzyme-mediated bioorthogonal cascade catalytic reaction for metabolism intervention and enhanced ferroptosis on neuroblastoma. *J. Am. Chem. Soc.* **146**, 8228–8241 (2024).
21. Du, K. et al. Aging promotes metabolic dysfunction-associated steatotic liver disease by inducing ferroptotic stress. *Nat. Aging* **4**, 949–968 (2024).
22. Noh B. et al. Iron overload induces cerebral endothelial senescence in aged mice and in primary culture in a sex-dependent manner. *Aging Cell* **22**, e13977 (2023).
23. Maus, M. et al. Iron accumulation drives fibrosis, senescence and the senescence-associated secretory phenotype. *Nat. Metab.* **5**, 2111–2130 (2023).
24. Admasu T. D. et al. Selective ablation of primary and paracrine senescent cells by targeting iron dyshomeostasis. *Cell Rep.* **42**, 112058 (2023).
25. Nousis, L., Kanavaros, P. & Barbouti, A. Oxidative stress-induced cellular senescence: is labile iron the connecting link?. *Antioxidants* **12**, 1250 (2023).
26. Lan M. et al. Photosensitizers for photodynamic therapy. *Adv. Healthcare Mater.* **8**, e1900132 (2019).
27. Shi, D. et al. Photoactivatable senolysis with single-cell resolution delays aging. *Nat. Aging* **3**, 297–312 (2023).
28. Vankayala, R. & Hwang, K. C. Near-infrared-light-activatable nanomaterial-mediated phototheranostic nanomedicines: an emerging paradigm for cancer treatment. *Adv. Mater.* **30**, e1706320 (2018).
29. Wan, Y., Fu, L. H., Li, C., Lin, J. & Huang, P. Conquering the hypoxia limitation for photodynamic therapy. *Adv. Mater.* **33**, e2103978 (2021).
30. Deng, X., Shao, Z. & Zhao, Y. Solutions to the drawbacks of photothermal and photodynamic cancer therapy. *Adv. Sci.* **8**, 2002504 (2021).
31. Zhao, H. et al. An energy-storing DNA-based nanocomplex for laser-free photodynamic therapy. *Adv. Mater.* **34**, e2109920 (2022).
32. Zhao, H. et al. Energy-storing DNA-based hydrogel remodels tumor microenvironments for laser-free photodynamic immunotherapy. *Biomaterials* **309**, 122620 (2024).
33. Gnaim, S. et al. Direct real-time monitoring of prodrug activation by chemiluminescence. *Angew. Chem. Int. Ed.* **57**, 9033–9037 (2018).
34. Jiang, G. et al. A selective and light-up fluorescent probe for β-galactosidase activity detection and imaging in living cells based on an AIE tetraphenylethylene derivative. *Chem. Commun.* **53**, 4505–4508 (2017).
35. Safir Filho, M., Dao, P., Gesson, M., Martin, A. R. & Benhida, R. Development of highly sensitive fluorescent probes for the detection of β-galactosidase activity – application to the real-time monitoring of senescence in live cells. *Analyst* **143**, 2680–2688 (2018).
36. Coffman, L. G., Parsonage, D., D'Agostino, R., Torti, F. M. & Torti, S. V. Regulatory effects of ferritin on angiogenesis. *Proc. Natl. Acad. Sci.* **106**, 570–575 (2009).
37. Lazar, A.-N., Perret, F., Perez-Lloret, M., Michaud, M. & Coleman, A. W. Promises of anionic calix[n]arenes in life science: State of the art in 2023. *Eur. J. Med. Chem.* **264**, 115994 (2024).
38. Ramberg, K. O., Engilberge, S., Skorek, T. & Crowley, P. B. Facile fabrication of protein–macrocycle frameworks. *J. Am. Chem. Soc.* **143**, 1896–1907 (2021).
39. Mester, L., Govyadinov, A. A., Chen, S., Goikoetxea, M. & Hillenbrand, R. Subsurface chemical nanoidentification by nano-FTIR spectroscopy. *Nat. Commun.* **11**, 3359 (2020).
40. Gnaim, S. et al. Light emission enhancement by supramolecular complexation of chemiluminescence probes designed for bioimaging. *Chem. Sci.* **10**, 2945–2955 (2019).
41. Yeung, J. Y. et al. Solvent-dependent supramolecular host-guest assemblies of platinum(II) tweezers and a guest system: from discrete molecules to high-ordered oligomers. *Angew. Chem. (Int. ed. Engl.)* **61**, e202207313 (2022).
42. Goudarzi, Z. et al. Two-dimensional polycyclodextrins for strong multivalent host-guest interactions at biointerfaces. *Small* **21**, e2412282 (2025).
43. Swain, S. et al. Photoactive nanocatalysts as DTT-assisted BSA-AuNCs with enhanced oxidase-mimicking ability for sensitive fluorometric detection of antioxidants. *J. Nanobiotechnol.* **22**, 585 (2024).
44. McKenna, E., Traganos, F., Zhao, H. & Darzynkiewicz, Z. Persistent DNA damage caused by low levels of mitomycin C induces irreversible cell senescence. *Cell Cycle* **11**, 3132–3140 (2014).
45. Liu, W. et al. Chlorin e6-biotin conjugates for tumor-targeting photodynamic therapy. *Molecules* **26**, 7342 (2021).
46. Cai, Y. et al. Elimination of senescent cells by β-galactosidase-targeted prodrug attenuates inflammation and restores physical function in aged mice. *Cell Res.* **30**, 574–589 (2020).
47. Zhang H. et al. Senolytic therapy enabled by senescent cell-sensitive biomimetic melanin nano-senolytics. *Adv. Healthc. Mater.* **13**, e2401085 (2024).
48. Raffaele, M. & Vinciguerra, M. The costs and benefits of senotherapeutics for human health. *Lancet Healthy Longev.* **3**, e67–e77 (2022).
49. Justice, J. N. et al. Senolytics in idiopathic pulmonary fibrosis: results from a first-in-human, open-label, pilot study. *EBioMedicine* **40**, 554–563 (2019).
50. Dhokia, V., Albati, A., Smith, H., Thomas, G. & Macip, S. A second generation of senotherapies: the development of targeted

senolytics, senoblockers and senoreversers for healthy ageing. *Biochem. Soc. Trans.* **52**, 1661–1671 (2024).
51. Chandrakar, L., Ambatwar, R. & Khatik, G. L. Cellular senescence and senolytic agents: recent updates on their role and applications. *Curr. Top. Med. Chem.* **24**, 157–178 (2024).
52. Sun, B., Bte Rahmat, J. N. & Zhang, Y. Advanced techniques for performing photodynamic therapy in deep-seated tissues. *Biomaterials* **291**, 121875 (2022).
53. Pezacki, A. T. et al. A tandem activity-based sensing and labeling strategy reveals antioxidant response element regulation of labile iron pools. *Proc. Natl. Acad. Sci.* **121**, e2401579121 (2024).
54. Zhang S. et al., Self-Illuminating NIR-II chemiluminescence nanosensor for in vivo tracking H2O2 fluctuation. *Adv. Sci.* **10**, 2207651 (2023).
55. Yang, S. et al. GSH/pH dual activatable cross-linked and fluorinated PEI for cancer gene therapy through endogenous iron de-hijacking and in situ ROS amplification. *Adv. Mater.* **36**, e2304098 (2023).
56. Nambiar, A. et al. Senolytics dasatinib and quercetin in idiopathic pulmonary fibrosis: results of a phase I, single-blind, single-center, randomized, placebo-controlled pilot trial on feasibility and tolerability. *eBioMedicine* **90**, 104481 (2023).
57. Guignabert, C. et al. Dasatinib induces lung vascular toxicity and predisposes to pulmonary hypertension. *J. Clin. Investig.* **126**, 3207–3218 (2016).
58. Delval, L. et al. Removal of senescent cells reduces the viral load and attenuates pulmonary and systemic inflammation in SARS-CoV-2-infected, aged hamsters. *Nat. Aging* **3**, 829–845 (2023).
59. Novais E. J. et al. Long-term treatment with senolytic drugs Dasatinib and Quercetin ameliorates age-dependent intervertebral disc degeneration in mice. *Nat. Commun.* **12**, 5213 (2021).
60. Budamagunta, V. et al. Senolytic treatment alleviates doxorubicin-induced chemobrain. *Aging Cell* **23**, e14037 (2024).

Acknowledgements

This work was supported by National Natural Scientific Funds (822770014 to L.Y.S., 82570028 to L.Y.S. and 81991523 to L.Y.S.), the National Key Research and Development Program Project (2018YFC1705900 to L.Y.S.), and the Contract Research (KHY0222601 to L.Y.S. and KHY0223601 to L.Y.S.).

Author contributions

L.Y.S., X.L.X. and C.P.W. conceived the conceptualization and designed the experiment; C.K.J., H.R.Z., C.J.C., L.Y.Z. and Z.Y.L, carried out the experiments; L.Y.S., X.L.X. and C.K.J. analyzed data and wrote the paper; N.Y., L.J.L. and S.M.C. contributed to scientific discussion of the article.

Competing interests

The authors declare no competing interests.

Additional information

Supplementary information The online version contains supplementary material available at https://doi.org/10.1038/s41467-025-67364-6.

Correspondence and requests for materials should be addressed to Xiaoling Xu, Chengping Wen or Liyun Shi.

Peer review information *Nature Communications* thanks Kaustabh Maiti, Mate Maus and the other anonymous reviewer for their contribution to the peer review of this work. A peer review file is available.